International Journal of Impact Engineering 196 (2025) 105156

Contents lists available at ScienceDirect

International Journal of Impact Engineering

journal homepage: www.elsevier.com/locate/ijimpeng

Low-velocity impact of castor oil-based rigid polyurethane foams: Experiments, microstructure effects and constitutive modelling

Jacopo Lavazza [a,*], Qicheng Zhang [a], Charles de Kergariou [a], Gianni Comandini [a], Fernando Alvarez-Borges [b], Orestis L. Katsamenis [b], Wuge H. Briscoe [c], Jemma L. Rowlandson [a,d], Tulio Hallak Panzera [e], Fabrizio Scarpa [a]

[a] Bristol Composites Institute, University of Bristol, Bristol, BS8 1TR, UK
[b] μ-VIS X-ray Imaging Centre, Faculty of Engineering and Physical Sciences, University of Southampton, Southampton, SO17 1BJ, UK
[c] School of Chemistry, University of Bristol, Cantock's Close, Bristol, BS8 1TR, UK
[d] School of Electrical, Electronic and Mechanical Engineering, University of Bristol, Bristol, BS8 1TR, UK
[e] Centre for Innovation and Technology in Composite Materials, Department of Mechanical and Production Engineering, Federal University of São João del Rei, São João del Rei, 36301-158, Minas Gerais, Brazil

ARTICLE INFO

Keywords:
Rigid polyurethane foam
Castor oil
Low-velocity impact
Micro CT
Hyperfoam model

ABSTRACT

Rigid polyurethane foams (RPUFs) are widely used in impact protection applications due to their tunable mechanical properties. Recently, RPUFs derived from bio-based sources such as castor oil have been investigated as a greener and more sustainable alternative to replace fossil-based polyurethane foams. It is thus important to understand the mechanical response of these materials to low-velocity impact (LVI), which still needs to be explored. This study aims to fill this gap by evaluating the performance of three types of RPUFs developed from commercially available castor oil-based resins. Drop weight impact tests at different impact energies were performed to investigate the LVI characteristics of the foams. Furthermore, an extensive micro-computed tomography investigation was carried out to improve the understanding of the microstructure of RPUFs and how the composition of these porous materials affected the foam architecture and the macroscopic mechanical response. Finally, a constitutive relationship is proposed to describe and predict the materials' response at different impact energies.

1. Introduction

Rigid polyurethane foams (RPUFs) are widely used in cushioning and packaging materials, impact and crash mitigation components, and sandwich structures because of their cellular architecture, low density and effectiveness in absorbing energy [1,2]. Cushioning materials must effectively dissipate kinetic energy while limiting the resulting impact force [3]. In these applications, these materials are typically subjected to low-velocity impact associated with drops [4]. Considerable efforts have been made to characterise the quasi-static and dynamic mechanical response of RPUFs to optimise their use. Chen et al. focused on the high strain rate response of RPUFs and found that the peak stress was affected by the strain rate and foam density [5]. Zhang et al. demonstrated the synergistic effect of RPUFs and the pyramidal lattice core on the load-bearing characteristics of sandwich panels under quasi-static compression and low-velocity impact [6]. Pellegrino et al. investigated syntactic polyurethane foams under strain rates ranging from 10^{-4} s^{-1} to 10^{3} s^{-1}, and observed the more pronounced foam sensitivity to the strain rate of foams compared to bulk materials [7]. Mane et al. further studied the effect of strain rate on RPUFs under quasi-static and dynamic compression (up to 160 s^{-1}). They observed an increase in energy absorption and the yield stress with increasing strain rate [8]. Hwang et al. showed how increasing density and decreasing temperature caused an increase of mechanical properties of the foams [9]. In contrast, the increase of impact energy resulted in densification [9]. Zhang et al. showed how minor variations of the strain rate induced considerable changes in the yield stress, plateau stress and energy absorption [10].

Polyurethane foams are obtained from the polyaddition reaction of polyols and isocyanates, derived entirely from petrochemicals. Driven

* Corresponding author.
E-mail addresses: jacopo.lavazza@bristol.ac.uk (J. Lavazza), qicheng.zhang@bristol.ac.uk (Q. Zhang), charles.dekergariou@bristol.ac.uk (C. de Kergariou), gianni.comandini@bristol.ac.uk (G. Comandini), f.j.alvarez-borges@soton.ac.uk (F. Alvarez-Borges), o.katsamenis@soton.ac.uk (O.L. Katsamenis), wuge.briscoe@bristol.ac.uk (W.H. Briscoe), j.rowlandson@bristol.ac.uk (J.L. Rowlandson), panzera@ufsj.edu.br (T.H. Panzera), f.scarpa@bristol.ac.uk (F. Scarpa).

https://doi.org/10.1016/j.ijimpeng.2024.105156
Received 26 June 2024; Received in revised form 26 September 2024; Accepted 24 October 2024
Available online 1 November 2024

by the ever-growing demand for green and more sustainable materials, recent studies have focused on alternative, bio-based sources of chemicals for the production of RPUFs [11,12]. Vegetable oils and, in particular, castor oil, are currently among the most investigated natural sources of polyols because of their abundance, low cost, biodegradability and ease of extraction [13]. In particular, castor oil naturally presents hydroxyl functionalities, making it a suitable polyol for RPUF synthesis without the need for chemical modifications and leading to its widespread as a green material [14]. Several studies have focused on chemical, physical and mechanical characterisation of castor oil-based RPUFs obtained at lab-scale [15–19]. More recently, Soares et al. and Lavazza et al. investigated castor oil-based RPUFs from commercial polyurethane resins, focusing on their structure–property relationship using a design of experiment approach [20] and an extensive multiscale experimental study [21]. On the other hand, only a limited number of studies have described the low-velocity impact (LVI) response of bio-based RPUFs. Mourão and Neto investigated castor oil-based RPUFs of densities from 0.043 to 0.277 g cm^{-3} subjected to drop impact tests performed at different strain rates, ranging from 130 to 318 s^{-1}. However, the different foams were evaluated at different strain rates, making it challenging to compare their mechanical response. Furthermore, limited details were provided about the chemical composition and structure of the foams used [22]. Recupido et al. produced RPUFs based on cashew nut oil and containing silica and hemp fibres. Low-velocity impact tests were performed at an impact energy of 1.2 J, limiting the scope of the investigation to an assessment of the effect of filler on the peak force registered during impact [12].

Cellular materials and foams are multiscale hierarchical systems [23]. It is well understood that the macroscopic mechanical behaviour is influenced by the foam microstructure and microstructural deformation mechanisms [24]. For this reason, different studies have focused on the application of in-situ micro-computed tomography (μCT) imaging to determine the foam microstructure evolution during compression [25–27]. On the other hand, in-situ μCT of dynamic events (such as low-velocity impact) require extremely accurate time resolution and remain difficult to achieve without the use of synchrotron-assisted experiments [28]. Determining the microscopic characteristics of foams after the impact event still provides insight into the hierarchical nature of these materials.

Driven by the lack of experimental data regarding the low-velocity impact behaviour of bio-based RPUFs, this work investigates the LVI response of three different foams obtained from various commercially available castor oil-based polyols and isocyanate mixtures. In particular, we consider the effect of the impact energy, ranging from 5 J to 30 J. The manuscript is structured as follows: in Section 2, the materials composition and density are reported, in addition to the details on the experimental methods employed (drop weight impact tests and μCT scan), and the analysis methods. Section 3 focuses on the macroscopic response of the three RPUFs, with the determination of the material parameters describing their dynamic mechanical and energy absorption characteristics. In Section 4, the details of the processing and analysis of the μCT scans are reported, in addition to the obtained results highlighting the microscopic effect of the low-velocity impact. Finally, a semi-empirical constitutive model is adapted to describe and predict the foams' crushing response, reported alongside its validation in Section 5.

2. Materials and methods

2.1. Materials

Three different castor oil (CO)-based rigid PUF formulations were studied in this work. Foam samples were obtained by mixing the Mamonex® RD70 A (RD A) isocyanate with CO additives, with two different polyester polyols derived from CO, namely Mamonex® RD70 B (RD B) and Imperveg® AGT 1315 B (AGT B), in three different mixing ratios listed in Table 1 and referred to as RF1, RF2, and RF3, respectively. All formulations were prepared by manually mixing polyols and isocyanate for about 1.5 min. The mixture was then poured into medium-density fibreboard moulds ($250 \times 250 \times 60$ mm^3) and cured for 14 days [20]. All the chemicals were supplied by Imperveg Polímeros Ind e Com (Brazil), and the foam samples were produced at the Federal University of São João del-Rei. No further details about additives used in the formulation were available from the supplier.

Table 1
Chemical formulation and apparent density (ρ) of the three foams characterised in the work.

Foam	RD A, [wt%]	RD B, [wt%]	AGT B, [wt%]	ρ, [g cm^{-3}]
RF1	60	40	0	0.08 ± 0.003
RF2	50	20	30	0.16 ± 0.007
RF3	50	40	10	0.09 ± 0.099

Table 2
Impact velocity (v) and strain rate ($\dot{\epsilon}$) for the different impact energies (J_i).

J_i, [J]	v, [m s^{-1}]	$\dot{\epsilon}$, [s^{-1}]
5	1.33	87 ± 2.91
10	1.88	123 ± 1.83
20	2.66	174 ± 5.01
30	3.26	214 ± 6.88

The apparent density (ρ, reported in Table 1) was determined as the mass-to-volume ratio of forty untested specimens for each foam. The specimens' dimensions were measured using a digital electronic vernier calliper (Siegen, UK) with an accuracy of ±0.01 mm and masses were measured with a Mettler Toledo XS203S XS balance (Mettler Toledo, Switzerland) with an accuracy of ±0.001 g.

The foam characteristics were evaluated along two material directions to identify possible anisotropy due to the foaming process. The foam rising direction is identified as d_r, whereas d_t refers to the transverse direction, normal to d_r.

2.2. Drop weight impact experimental setup

The low-velocity impact response of the foams was determined through drop impact tests, performed via an Instron® 9450 drop tower (Instron Corporation, USA), show in Fig. 1. The machine was equipped with a C-7529-302 strain gauge tup (or impactor) with a capacity of 45 kN and a C-7529-350 flat-faced circular insert (diameter of 50 mm). The impact force signal was obtained from the strain gauge tup, whereas the displacement signal was recorded via a photocell. The total drop mass was 5.6 kg. Four different impact energies (J_i) corresponding to 5, 10, 20, and 30 J were adopted for testing by varying the drop height of the weight. The drop weight velocity before impact (v) was determined from the photocell. The velocity and strain rate ($\dot{\epsilon} = v/h_0$, where h_0 is the initial specimen thickness) corresponding to each J_i are reported in Table 2.

Impact tests were performed on rectangular specimens of $30 \times 30 \times 15$ mm^3 in size [29], obtained using a hot-wire cutter. Five specimens for all foams were tested in each impact energy condition for both material directions d_i (d_r and d_t; see Section 2.1). A Photron fastcam SA-Z high-speed camera (Photron, Japan) equipped with a 100 mm F2.8 Macro AT-X ProD lens (Tokina Co., Japan) and with a framerate of 70,000 s^{-1} was used to video record the macroscopic specimen deformation, as shown in Fig. 1. The camera was positioned at approximately 0.5 m from the samples.

2.3. Micro-computed tomography scans

Micro-computed tomography (μCT) scans were used to characterise the foam microstructure and its morphological characteristics. The μCT scans were obtained using a customised Nikon XRH XT H 225 ST X-ray tomography scanner (Nikon X-Tek Systems Ltd, UK), equipped with a

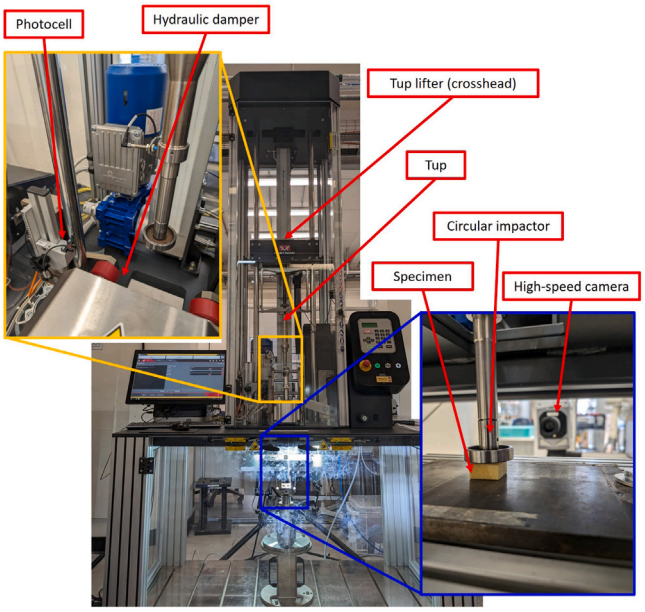

Fig. 1. Drop weight impact experimental setup: drop tower with main components indicated, foam specimens and high-speed camera position.

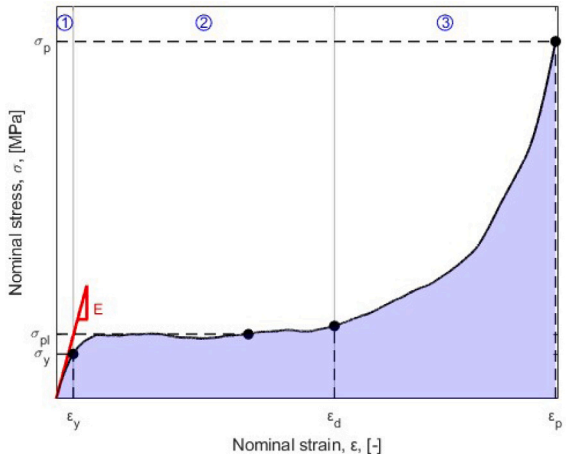

Fig. 2. Generic loading stress–strain curve for an RPUF in compression, with indication of the three regions of the response: (1) linear elastic, (2) plateau, (3) densification. Parameters discussed in Section 3.1: compressive modulus (E), yield stress (σ_y) and strain (ε_y), plateau stress (σ_{pl}), densification strain (ε_d), peak stress (σ_p) and strain (ε_p), and energy absorbed per unit volume (EA, blue area).

sample exchange autoloader system [30]. Scans were performed with an angular step of 0.11°, acquiring a total of 4001 projections throughout a full 360° rotation of the object. Each projection was recorded as the average of 8 frames, with an exposure time of 177 ms per frame. The accelerating voltage of the X-ray tube was 80 kV, and the beam current value was equal to 94 μA. The source-to-object and source-to-detector distances were set to 37.5 mm and 937.5 mm, respectively, yielding an isotropic voxel edge size of 6 μm. Scans were performed on cubic samples approximately $10 \times 10 \times 10$ mm^3 in size, obtained from the central region of the impacted samples. Specimens tested in each impact energy condition (see Section 2.2) for both material directions for each foam type were analysed. Tomographic reconstruction was carried out using the Nikon CT Pro 3D (Nikon Metrology, UK) software package, which uses a filter-back projections algorithm.

2.4. Determination of the Poisson's ratio

The Poisson's ratio (ν) is defined as the ratio between the in-plane transverse (ε_2) and longitudinal (ε_1) nominal strains [31]. For foams, the value of ν depends on the strain level considered, and it is not an absolute material constant [32]. The constitutive model presented in Section 5.1 is based on the generalised Poisson ratio (ν_0), or the value of ν for infinitesimal strains as defined in Eq. (1):

$$\nu_0 = \nu(\varepsilon_1 \to 0) = -\left.\frac{\varepsilon_2}{\varepsilon_1}\right|_{\varepsilon_1 \to 0} \tag{1}$$

The Poisson's ratio as a function of ε_1 of the three foams was determined from the recorded images of the specimens' deformation during impact (up to $\varepsilon_1 \approx 50\%$). Image analysis was performed using the software Fiji/ImageJ [33] by thresholding the images and measuring the width and height variations of the obtained mask. The generalised Poisson's ratio cannot be determined experimentally. Therefore, the value of ν_0 was extrapolated in MATLAB through a third-order polynomial fitting of the measured values. The deformation images of five samples per foam, in each material direction, were analysed.

2.5. Statistical analysis of the data

The MATLAB function `anova` was used to perform one-way analysis of variance (ANOVA) to compare the statistical performance of the measured data. Data sets are considered statistically equivalent if $p > 0.05$ (i.e., they have a 5% or less chance of being statistically different). In ANOVA studies, the $F(k-1, N-k)$ values given represent the ratio of the variance between the group compared and the variance within the groups compared. k is the number of data groups compared, and N is the total number of values considered in the groups compared. As a consequence, the higher the F value, the more different the different values are [34].

3. Impact performance of the foams

3.1. Parameters describing the impact performance

The impact behaviour of the foams is described in terms of nominal stress (σ) and nominal strain (ε), obtained from the force and displacement signals. The raw data was smoothed through a Savitzky–Golay filter (`sgolayfilt` function in MATLAB with order set to 3 and frame length set to 501) to reduce experimental noise. In the following, both σ and ε are considered positive in compression. The typical impact stress–strain curve of RPUFs is reported in Fig. 2. The energy absorption characteristics are determined by the specific energy absorption (SEA) [35] according to Eq. (2):

$$SEA = \frac{1}{\rho}\int_0^{\varepsilon} \sigma(\varepsilon)d\varepsilon = \frac{EA}{\rho}, \tag{2}$$

In Eq. (2), EA is the energy absorption per unit volume and ρ is the apparent density. The energy absorption efficiency (efficiency, U_e) was proposed to evaluate the energy absorption characteristics of porous materials [3,36], and is defined in Eq. (3):

$$U_e = \frac{1}{\sigma(\varepsilon)}\int_0^{\varepsilon} \sigma(\varepsilon)d\varepsilon = \frac{EA}{\sigma(\varepsilon)}. \tag{3}$$

The stress–strain curves of RPUFs subjected to low-velocity impact show three distinct regions of the material response (highlighted in Fig. 2), which correspond to linear elastic, plateau, and densification regions [9] (further discussed in Section 3.2). The material response in the linear elastic region is quantified by the compressive modulus (E), calculated as the tangent modulus at $\varepsilon = 2\%$ from Eq. (4):

$$E = \left.\frac{d\sigma(\varepsilon)}{d\varepsilon}\right|_{\varepsilon=2\%}. \tag{4}$$

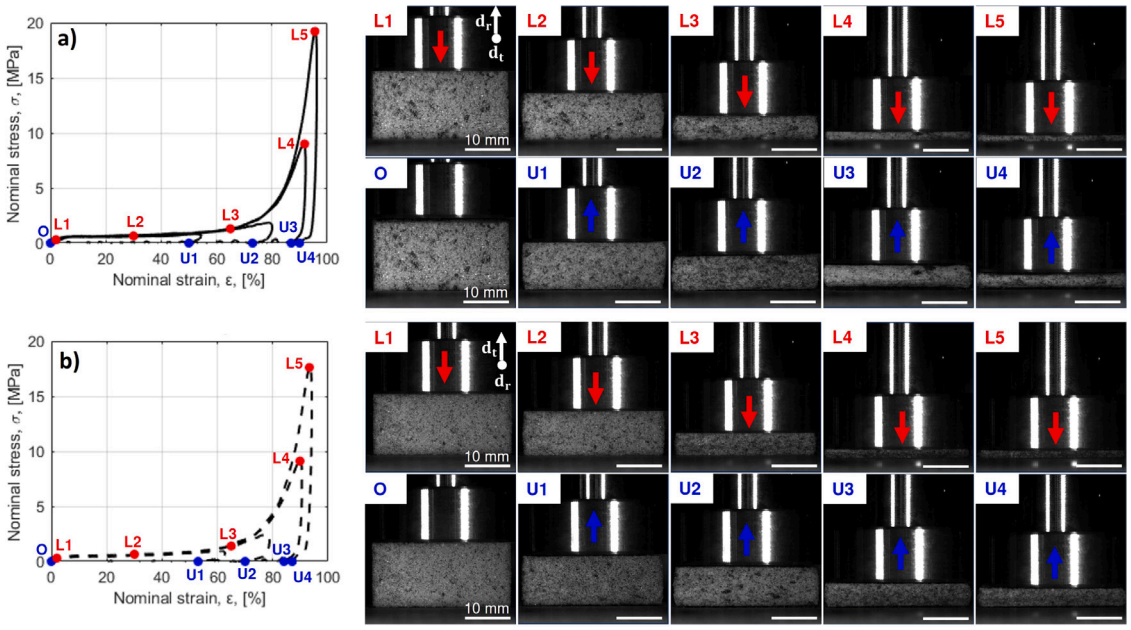

Fig. 3. Nominal stress–strain ($\sigma-\varepsilon$) curves (loading and unloading) for RF1 subjected to different impact energies (J_i = 5, 10, 20, and 30 J) for the: (a) rise (d_r) and (b) transverse (d_t) direction. Corresponding images at significant points of the loading (labelled as L) and unloading (labelled as U) cycle, and at the start point of the impact (labelled O). The scale bar is 10 mm for all the images.

The densification strain (ε_d) represents the upper limit of the plateau region. It is defined as the strain at which the energy absorption efficiency reaches a maximum [37], satisfying Eq. (5):

$$\left.\frac{dU_e}{d\varepsilon}\right|_{\varepsilon=\varepsilon_d} = 0. \tag{5}$$

The plateau stress (σ_{pl}) characterises the plateau region and is defined from Eq. (6) [38]:

$$\sigma_{pl} = \frac{1}{\varepsilon_d - \varepsilon_y}\int_{\varepsilon_y}^{\varepsilon_d} \sigma(\varepsilon)d\varepsilon, \tag{6}$$

In Eq. (6), ε_y is the strain corresponding to the yield stress (σ_y), which identifies the upper limit of the linear elastic region. Note that the yield point was identified here by following the tangent method reported previously by Viot [39]. The peak stress (σ_p) is defined as the maximum stress upon impact, whereas the peak strain (ε_p) is the maximum strain reached during the test.

3.2. Drop weight impact response

The typical stress–strain curves for RF1 in the rise and transverse directions subjected to the different impact energies (J_i = 5, 10, 20, and 30 J) are reported in Fig. 3, alongside the video-recorded images at significant stages of the macroscopic deformation process. As expected [9], the extent of the material response investigated increases with increasing impact energy. The linear elastic region (identified by point L1) is limited to strains lower than 5%, and the stress linearly increases with the strain up to the yield point.

Microscopically, cell walls deform by bending and stretching in a fully reversible way [40]. For larger strains, the plateau response is observed (identified by point L2) where the stress level remains almost constant and corresponds to the gradual collapse of cell walls due to buckling and damage [41,42]. Upon reaching the densification strain (identified by point L3), cell walls start coming into contact with one another, resulting in a steep stress increase [43]. Increasing the impact energy from 20 J to 30 J leads to different peak stresses (points L4 and L5, respectively) because of the increased deformation and densification of the sample. After reaching the peak, the specimens are unloaded because of the drop weight rebound, and the residual deformation increases with increasing J_i (labelled as U1 for J_i = 5 J, U2 for J_i = 10 J, U3 for J_i = 20 J, and U4 for J_i = 30 J). The microstructural characteristics of the unloaded specimens will be discussed in Section 4.2.

Representative stress–strain curves of the three foams in the two material directions subjected to the different impact energies are reported in Fig. 4. While RF1 and RF3 present similar responses at every imposed energy level, the RF2 foam is stiffer (in the linear elastic region) and less deformable than the other foams. From a qualitative standpoint, this can be observed from Fig. 4 in which the curves of RF2 lie above the other ones for a fixed J_i and the unloading stage is reached at lower strains. These results agree with the quasi-static compression curves reported by Lavazza et al. for the same types of foams [21]. These differences can be explained in terms of the porosity of the three different foams at the microscopic scale (as further discussed in Section 4.2) [21], related to the apparent density at the macroscopic level (see Table 1) [9].

To quantify the response within the linear elastic region, the compression modulus (E) and the yield stress (σ_y) were determined as described in Section 3.1 for the different impact energies; their values are reported in Fig. 5. In the case of J_i = 5 J, it can be observed how both the E and σ_y values for both the rise and transverse directions are higher for RF2 compared to RF1 and RF3, which present comparable values. The ANOVA coefficients (see Section 2.5) for J_i = 5 J, considering the modulus of all foams and both directions are $F(5,24) = 20.75$ and $p = 5.26\times10^{-8}$.

Focusing on J_i = 5 J, in agreement with previous results [21], anisotropy of E is observed among the rise and transverse directions in the RF1 ($F(1,8) = 36.45$, $p = 3.1\times10^{-4}$) and RF3 ($F(1,8) = 13.54$, $p = 6.22\times10^{-3}$) foams. These results are most likely related to the elongation of the foam pores along the rise direction during the foaming reaction (as discussed in Section 4.2). Conversely, RF2 presents comparable stiffness in both directions ($F(1,8) = 1.21$, $p = 0.3$), possibly related to more spherical and less directionally-shaped pores. The same trends are observed for the yield stress for J_i = 5 J ($F(5,24) = 108.9$, $p = 1.1\times10^{-15}$), with RF2 presenting the highest value and an isotropic response ($F(1,8) = 1.52$, $p = 0.25$), followed by RF1 ($F(1,8) = 12.64$, $p = 7.46\times10^{-3}$) and RF3 ($F(1,8) = 5.83$ and $p = 0.042$), presenting higher values of σ_y in the rise direction.

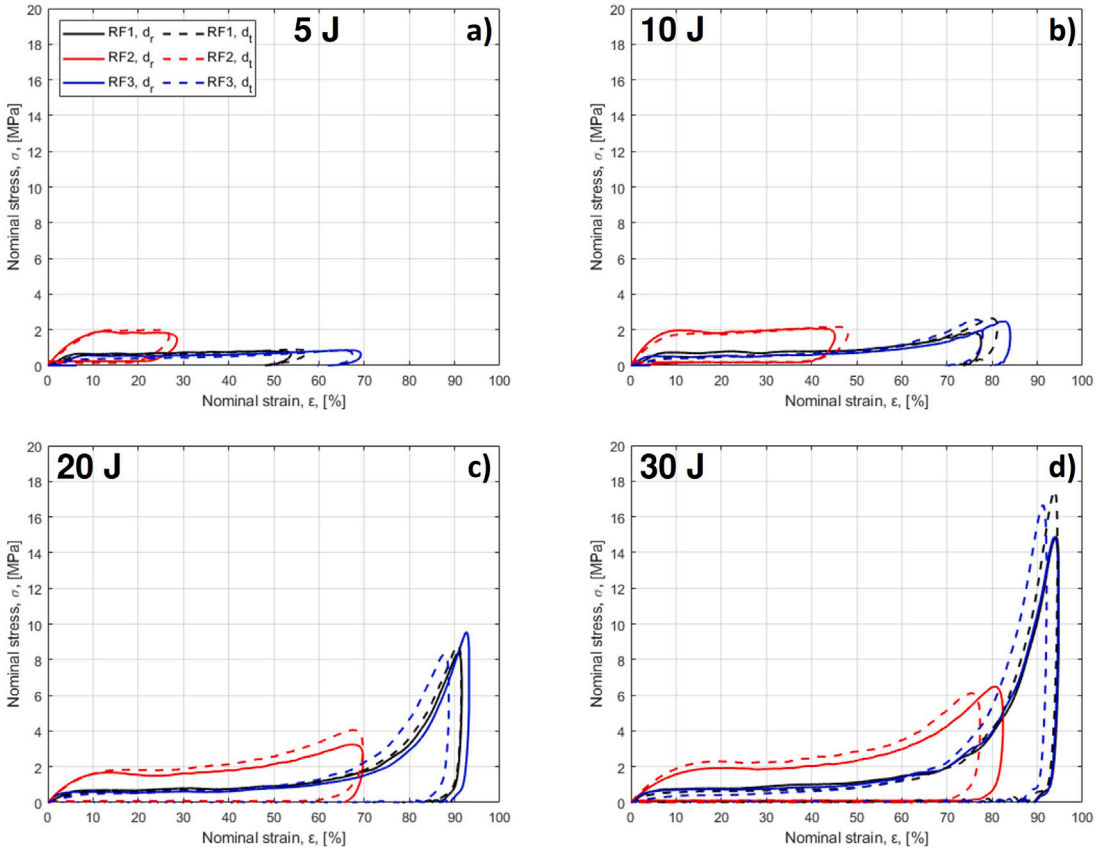

Fig. 4. Nominal stress–strain ($\sigma - \varepsilon$) curves (loading and unloading) for the three foams (RF1, RF2, and RF3) in the rise (d_r) and transverse (d_t) direction, subjected to different impact energies (J_i): (a) 5 J, (b) 10 J, (c) 20 J, and (d) 30 J. The legend is common to all plots.

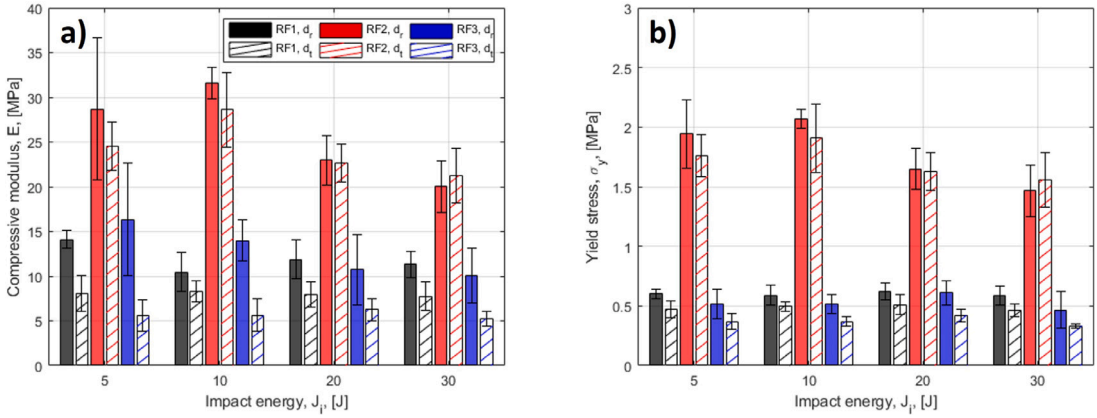

Fig. 5. Properties of the foams (RF1, RF2, RF3) in the rise (d_r) and transverse (d_t) direction, subjected to different impact energies (J_i): (a) compressive modulus (E), (b) yield stress (σ_y). The legend is common to all plots.

Similar trends of E and σ_y are observed for all impact energies, where RF2 presents the highest values and a comparable response in both material directions, followed by RF1 and RF3, which are characterised by higher values along d_r than d_t.

As a consequence of the different imposed impact energies, samples were subjected to different impact velocities (v) and strain rates ($\dot{\varepsilon}$) as reported in Table 2. The materials' compressive modulus and yield strength do not show a clear dependence on the imposed strain rate in the range investigated. For example, considering RF1 in direction d_t at the different J_i, the ANOVA coefficients are $F(3, 16) = 0.13$ and $p = 0.94$ for E, and $F(3, 16) = 0.61$ and $p = 0.62$ for σ_y. This is in agreement with previous studies that have highlighted how only the increase of orders of magnitude in the strain rate can lead to an increase of the yield point [2,8,9], whereas significant variations of the compressive modulus are observed in very rapid dynamic events ($\dot{\varepsilon} \geq 250\ s^{-1}$) [38].

At large strains, the response in the plateau and densification regions is quantified by metrics like the plateau stress (σ_{pl}), densification strain (ε_d), peak stress (σ_p) and peak strain (ε_p). All these quantities were determined as described in Section 3.1 and reported as a function of the impact energy in Fig. 6. Note that the plateau stress and densification strain were determined only for RF1 and RF3 for $J_i = 10$ J. This is because the definition of ε_d (see Eq. (5)) requires the efficiency to reach a maximum value. Because of the less deformable nature of RF2, this maximum is reached only for higher impact energy levels (see Fig. 4). Similarly, for $J_i = 5$ J, none of the foams reach the densification

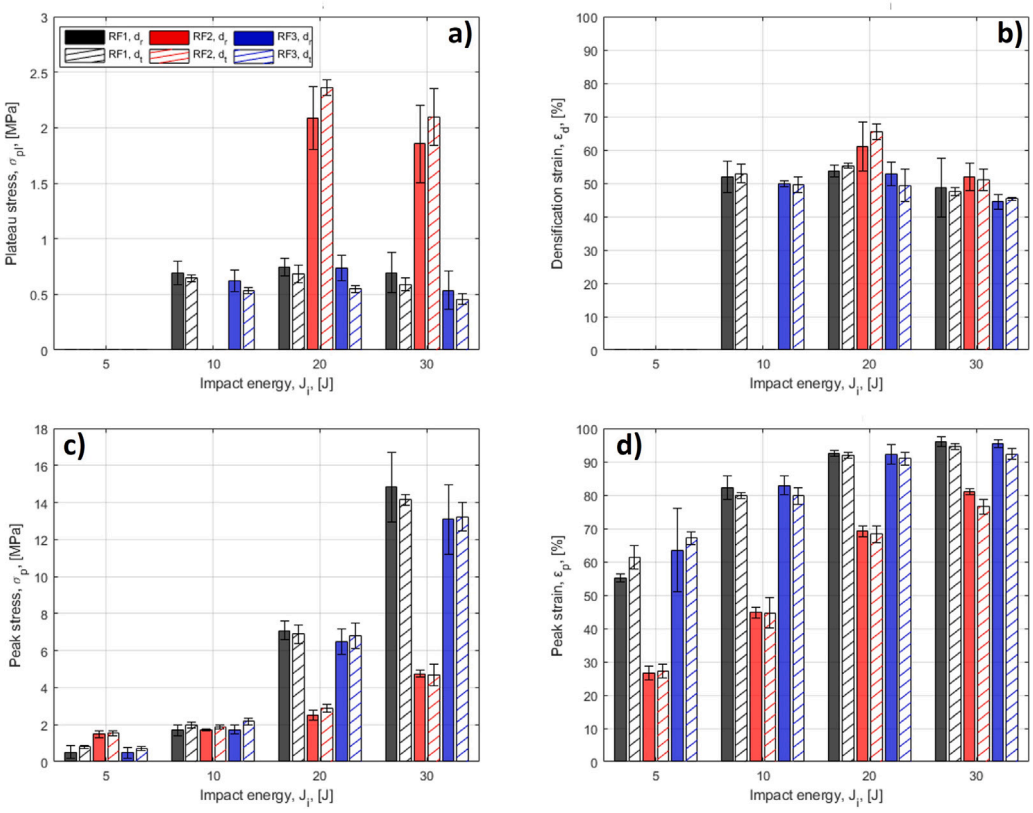

Fig. 6. Properties of the foams (RF1, RF2, and RF3) in the rise (d_r) and transverse (d_t) direction, subjected to different impact energies (J_i): (a) plateau stress (σ_{pl}), (b) densification strain (ε_d), (c) peak stress (σ_p), and (d) peak strain (ε_p). The legend is common to all plots.

stage. The σ_{pl} definition (see Eq. (6)) is based on the identification of the densification strain; therefore, the same considerations apply.

From Fig. 6.(b) it can be observed that RF1 shows comparable densification strains for both the rise and transverse directions and that ε_d is not significantly affected by the value of the impact energy ($F(5,24) = 2.39$ and $p = 0.067$). On the other hand, RF2 and RF3 show the highest densification strains for $J_i = 20$ J ($F(3,16) = 11.38$ and $p = 3 \times 10^{-4}$ for RF2; $F(5,24) = 6.2$ and $p = 7 \times 10^{-4}$ for RF3). Similar trends are observed for the plateau stresses (see Fig. 6.(a)), whose definition depends on the value of ε_d. The plateau stress and densification strain for all foams present comparable values along the two materials' directions. The disappearance of mechanical anisotropy at large strains can be attributed to the porous microstructure of the foams and the definition of densification strain, that is, the strain at which the cell walls come into contact [37]. Therefore, the pore elongation and size are reduced, resulting in a more isotropic response [44]. Furthermore, RF2 shows a significantly higher value of σ_{pl} than RF1 and RF3, most likely related to its higher density. Similarly, the value of ϵ_d is higher for RF2 than RF3, although it is statistically comparable to that of RF1 (for $J_i = 20$ J, $F(5,24) = 10.5$ and $p = 2 \times 10^{-5}$).

The values of peak stress and peak strain are comparable in the different material directions at all energy levels (see Fig. 6.(c–d)). Both σ_p and ε_p increase with increasing J_i for all the foams. For $J_i = 5$ J, the plateau stress identifies the peak stress since full densification is not reached for this energy level; therefore, RF2 presents a higher σ_p value than RF1 and RF3. With increasing energy levels, the peak stress of RF2 becomes lower than those of the other two foams. For $J_i = 10$ J, the σ_p value of RF1 and RF3 corresponds to the onset of the densification stage, while RF2 is still in the plateau region. For higher energy levels, the σ_p value of RF1 and RF3 corresponds to a significant densification of their structure. In contrast, the extent of the crushing of RF2 is more limited, as it can be noticed by the trends of ε_p and from the stress–strain curves reported in Fig. 4.

Table 3
Specific modulus (E/ρ), specific yield stress (σ_y/ρ), and specific plateau stress (σ_{pl}/ρ) for the three foams (RF1, RF2, RF3) in the rise (d_r) and transverse (d_t) direction (d), at an impact energy (J_i) of 30 J.

Foam	d	E/ρ, [MPa cm^3 g^{-1}]	σ_y/ρ, [MPa cm^3 g^{-1}]	σ_{pl}/ρ, [MPa cm^3 g^{-1}]
RF1	d_r	146 ± 10.4	7.61 ± 0.56	9.02 ± 1.77
	d_t	98.6 ± 22.1	5.86 ± 0.73	7.62 ± 0.75
RF2	d_r	130 ± 17.2	9.48 ± 1.32	12.1 ± 2.18
	d_t	125 ± 17.1	9.18 ± 1.24	12.5 ± 1.34
RF3	d_r	118 ± 18.7	5.43 ± 0.91	6.31 ± 0.98
	d_t	57.9 ± 11.9	3.57 ± 0.34	5.16 ± 0.14

The three foams present different apparent densities (ρ) as a consequence of their different chemical composition (see Table 1). For this reason, their impact performance can be further compared through the specific impact properties (i.e., the properties normalised by ρ). In particular, the compressive modulus, yield stress, and plateau stress do not show statistically significant variations with the impact energy. In Table 3 the values of specific modulus (E/ρ), specific yield stress (σ_y/ρ), and specific plateau stress (σ_{pl}/ρ) are reported for $J_i = 30$ J. In particular, the value of specific modulus are comparable for all foams and directions ($F(5,24) = 17.1$ and $p = 3.2 \times 10^{-7}$), with the only exception of RF3, d_t which is lower than the others. On the other hand, the values of σ_y/ρ and σ_{pl}/ρ follow those already described in this section, with RF2 presenting higher values than RF1 and RF3.

3.3. Energy absorption characteristics

The specific energy absorption (SEA, see Eq. (2)) is a fundamental parameter in determining the impact performance of materials, quantifying the kinetic energy absorbed and dissipated. In the case of RPUFs, the kinetic energy is converted through microstructural mechanisms

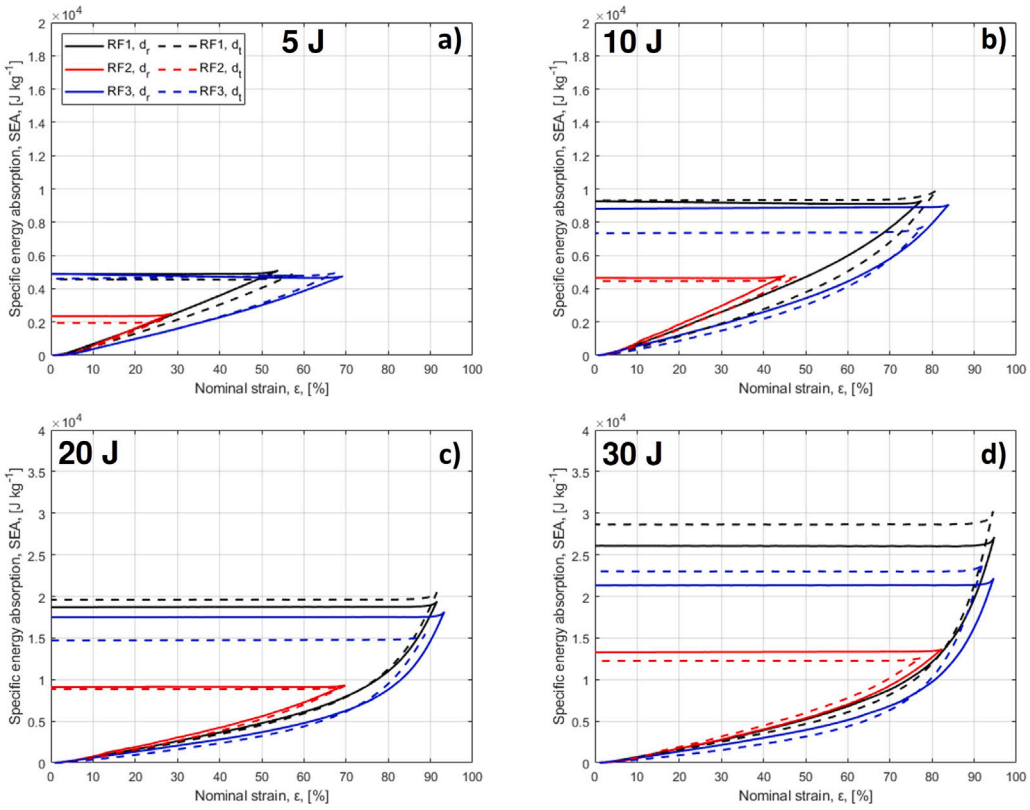

Fig. 7. Specific energy absorption-nominal strain ($SEA-\varepsilon$) curves (loading and unloading) for the three foams (RF1, RF2, and RF3) in the rise (d_r) and transverse (d_t) direction, subjected to different impact energies (J_i): (a) 5 J, (b) 10 J, (c) 20 J, and (d) 30 J. The legend is common to all plots. Note that the scale of (a) and (b) differs from (c) and (d).

such as bending and buckling of cell walls [45]. Representative SEA curves as a function of nominal strain for the three foams in the two material directions for the different J_i are reported in Fig. 7.

The SEA curves reach higher values and extend to larger strains with increasing J_i (as reflected from the σ_p and ε_p values reported in Fig. 6). The curves of RF1 and RF3 at $J_i = 20$ and 30 J present a peak of SEA at the peak strain, which rapidly decreases in a span of approximately 5% strain corresponding to the unloading region, to then stabilise at a constant value which indicates the complete unloading of the specimen (see Fig. 7.(c–d)). Furthermore, the loading curves corresponding to RF2 lie above the ones of RF1 and RF3 (see Fig. 7), indicating increased energy absorption capabilities with increasing density (see Table 1), as already reported in previous studies [9].

The maximum admissible load is generally defined as that at the end of the plateau region, in correspondence with the densification strain [46]. For this reason and previous considerations reported in Section 3.2, the maximum SEA (in correspondence of ε_d) value can be defined for $J_i = 10$, 20 and 30 J for RF1 and RF3, and for $J_i = 20$ and 30 J for RF2. The values of SEA at the densification strain for the three foams in the two materials directions are summarised in Table 4. RF2 presents the highest SEA value for a fixed impact energy, followed by RF1 and RF3. Furthermore, RF1 presents comparable values for both directions and all J_i (from ANOVA, $F(5,24) = 1.04$, $p = 0.42$). RF3 presents the highest SEA for $J_i = 20$ J in the rise direction, whereas all other values are comparable for both directions and all impact energies ($F(5,24) = 6.9$, $p = 4 \times 10^{-4}$). On the other hand, RF2 presents comparable values in the two material directions, but the SEA is consistently higher for $J_i = 20$ J than $J_i = 30$ J ($F(3,16) = 9.18$, $p = 9 \times 10^{-4}$).

The energy absorption efficiency (U_e, see Eq. (3)) is another parameter introduced to evaluate the energy absorption characteristics of cellular materials. The efficiency at a certain strain $\bar{\varepsilon}$ represents the ratio between the energy absorbed by the real foam specimen, compared to an ideal one which transmits the same but constant stress $\bar{\sigma}$ (corresponding to the same strain $\bar{\varepsilon}$) [36]. The efficiency varies between 0 and 1, where the latter identifies an ideal foam. Representative U_e curves as a function of nominal stress for the three foams in the two material directions for the different J_i are reported in Fig. 8.

Table 4
Specific energy absorption (SEA, all values in J g^{-1}) at the densification strain (ε_d) for the three foams (RF1, RF2, RF3) in the rise (d_r) and transverse (d_t) direction (d), for the different impact energies (J_i).

Foam	d	J_i, [J]			
		5	10	20	30
RF1	d_r	–	4.72 ± 0.79	5.30 ± 0.31	4.91 ± 1.74
	d_t	–	4.51 ± 0.43	5.11 ± 0.29	4.27 ± 0.4
RF2	d_r	–	–	7.79 ± 1.22	6.15 ± 0.45
	d_t	–	–	8.46 ± 0.3	6.41 ± 0.93
RF3	d_r	–	3.61 ± 0.29	4.17 ± 0.58	3.40 ± 0.25
	d_t	–	3.05 ± 0.24	3.31 ± 0.47	3.02 ± 0.13

Of particular interest is the maximum efficiency value, which corresponds to the densification strain (see Eq. (5)). A maximum value can be defined for all examined impact energies. However, it does not mean the densification strain can be defined for all impact cases, as discussed in Section 3.2. No significant variations are observed in maximum U_e with varying J_i. The main parameter affecting the position of the peak is the material apparent density, which shifts the maximum to higher stresses (and lower strain) when ρ is higher, in the case of RF2 (see Table 1). This result is a consequence of the plateau stress and densification strain considerations reported in Section 3.2. The maximum values of U_e for the three foams in the two materials directions are summarised in Table 5.

Whilst RF1 and RF3 show consistent results across the different impact energies, RF2 presents an increase in the maximum efficiency with increasing J_i because the material does not reach the densification

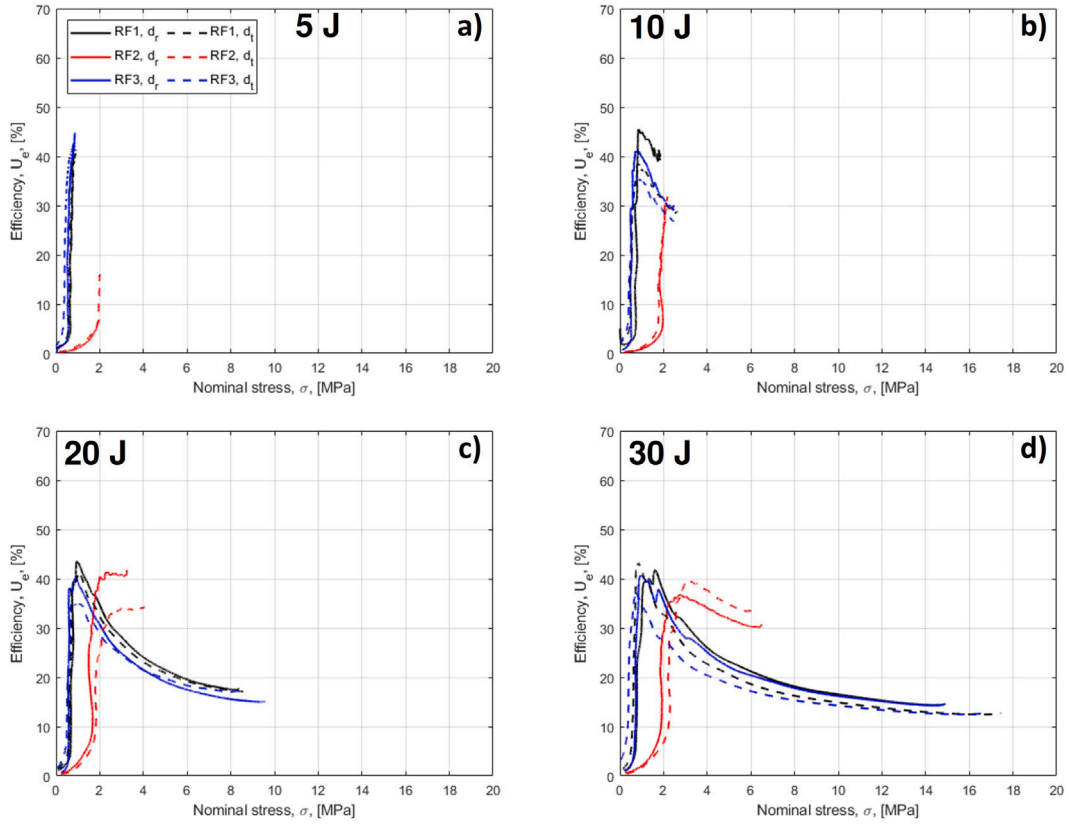

Fig. 8. Efficiency-nominal stress ($U_e - \sigma$) curves (loading) for the three foams (RF1, RF2, and RF3) in the rise (d_r) and transverse (d_t) direction, subjected to different impact energies (J_i): (a) 5 J, (b) 10 J, (c) 20 J, (d) 30 J. The legend is common to all plots.

Table 5
Maximum energy absorption efficiency (U_e, all values in %) for the three foams (RF1, RF2, RF3) in the rise (d_r) and transverse (d_t) direction (d), for the different impact energies (J_i).

Foam	d	J_i, [J]			
		5	10	20	30
RF1	d_r	44.4 ± 2.84	43.8 ± 1.61	43.2 ± 1.38	45.4 ± 3.63
	d_t	42.5 ± 1.64	39.4 ± 2.03	39.7 ± 1.06	42.0 ± 2.38
RF2	d_r	6.40 ± 1.05	28.0 ± 1.59	42.2 ± 3.24	39.7 ± 5.44
	d_t	15.0 ± 4.66	28.1 ± 4.13	36.3 ± 1.77	38.5 ± 2.87
RF3	d_r	45.6 ± 4.56	42.1 ± 1.71	39.1 ± 2.75	45.8 ± 5.6
	d_t	41.7 ± 3.25	36.0 ± 2.29	38.6 ± 3.18	40.7 ± 3.82

point for lower impact energies. Furthermore, at $J_i = 5$ J, RF1 and RF3 do not present the decreasing trend observed after the U_e maximum. The maximum efficiency does not correspond to the densification strain in these cases.

RF1 presents an efficiency of approximately 44% in the rise direction and 41% in the transverse direction, with negligible variations with J_i although the U_e values in d_t for $J_i = 10$ J and $J_i = 20$ J are marginally lower than the others (from ANOVA, $F(7, 32) = 4.66$ and $p = 1 \times 10^{-3}$). Similar trends are observed for RF3 ($F(7, 32) = 4.41$ and $p = 1 \times 10^{-3}$), and the maximum values are approximately 43% in d_r and 39% in d_t. As already mentioned, RF2 shows an increasing trend of efficiency with impact energy ($F(7, 32) = 69.8$ and $p = 1 \times 10^{-17}$), ranging from approximately 6% for $J_i = 5$ J to 40% for $J_i = 20$ J and $J_i = 30$ J. Furthermore, the maximum value in the transverse direction is more than twice that in the rise direction. It should be noted that the efficiency of the foams under investigation is higher or comparable than previous works on petroleum-based RPUFs: Xiao et al. reported values of 44% for quasi-static and 36% for high strain rate (2500 s^{-1}), highlighting the effect of strain rate on U_e [46]; Xing et al. reported a maximum value of approximately 35% for quasi-static compression tests [35].

4. Effect of impact on the foams' microstructure

4.1. Micro-computed tomography processing and analysis

RPUFs present a multiscale hierarchical structure: in Sections 3.2 and 3.3, the results presented and discussed focused on the macroscopic (length scale larger than 1 mm) material response, described in terms of stress and strain. As already discussed, the RPUFs' distinctive mechanical behaviour is a consequence of their cellular structure: at the microscopic scale (dimensions ranging from 1 μm to 1 mm), the foams present closed pores containing gasses derived from the foaming reaction, separated by an interconnected network of polymeric ribs (or struts). As already observed in Fig. 3, different residual deformations correspond to different imposed impact energy levels. Analysing the microstructure of the samples after impact through micro-computed tomography (μCT) makes it possible to correlate microscopic parameters to the macroscopic response.

The μCT reconstruction and analysis procedure is shown in Fig. A.1 in Appendix A. The scanned volumes were processed via the software Comet Dragonfly 2022.2.0 (Comet Technologies Canada Inc., Montreal, Canada). A median filter (square kernel, 3 px in size) was applied to the original volumes. Sub-volumes 500 × 500 × 500 voxels in size (corresponding to 3×3×3 mm^3) were obtained from the central region of the original volumes by manual cropping. The sub-volumes were employed for ease of analysis and reduced computational time. Binary segmentation was performed by automatic thresholding (using the built-in Otsu method [47]) to selected levels and obtaining the polymeric ribs and pore space. Watershed segmentation [48] was employed to identify and separate the individual pores. The pore radius (R) and sphericity (Ψ)

were determined using built-in features of the Dragonfly software. The pore radius reported in the following discussion is the mean radius, quantifying the mean distance between the centroid and the pore's surface. The sphericity describes how closely a pore approaches the mathematically ideal sphere [49] and is defined in Eq. (7):

$$\Psi = \frac{\pi^{\frac{1}{3}} \left(6V_p\right)^{\frac{2}{3}}}{A_p}, \tag{7}$$

where V_p is the pore volume, and A_p is the pore surface area. Because of its definition, Φ varies between 0 (a line) and 1 (a perfect sphere). The rib space was skeletonised and converted into a sparse graph, identifying the nodes and connections of the rib network. From the skeleton and nodes definition, the geometrical tortuosity (τ) of the ribs was defined following Eq. (8):

$$\tau = \frac{C}{L}, \tag{8}$$

where C is the length of the curved rib, and L is the distance between two rib ends (i.e., the Euclidean norm) [50]. Finally, the porosity (ϕ) was calculated as the ratio between the black pixels (corresponding to the pore space) and the total number of pixels in each sub-volume.

4.2. Microstructure evolution upon impact

The scanned volume of RF1 in the rise direction (d_r) subjected to $J_i = 5$ J was divided into eight sub-volumes (called S1 to S8), which were not overlapping with one another, to verify the accuracy and significance of the measurements performed onto the sub-volumes. The probability distributions of ribs tortuosity, pore radius, and pore sphericity are reported in Fig. A.2, and the calculated porosity values are reported in Table A.1 in Appendix A.

The probability distributions for τ, R, and Ψ show similar characteristics among all analysed sub-volumes, with minor differences related to some limited statistical variability of the analysed volume morphology. Furthermore, all sub-volumes show comparable porosity degrees, with a standard deviation of approximately 0.2% (see Table A.1). It should be noted that ANOVA (see Section 2.5) could not be applied to statistically compare the morphological properties since a different number of measurements was obtained from each sub-volume. Nonetheless, it was concluded that using sub-volumes 500 × 500 × 500 voxels in size was a sufficient approximation of the whole volume characteristics while also reducing the computational times of the analysis. Therefore, for every testing condition, only one sub-volume obtained from the total volume's central region was analysed and is referred to in the following discussion.

The μCT sub-volumes for the three foams, in both directions (rise and transverse), subjected to $J_i = 5$, 10, 20, and 30 J are reported in Fig. 9.(a). The microscopic sub-volumes correspond to the unloading points reported in Fig. 3 (labelled U1 to U4). For RF1 and RF3, it is possible to see that the foam microstructure becomes denser with increasing impact energy and the pores get increasingly crushed. In fact, for $J_i \geq 20$ J, the materials reach the densification stage of their response. RF2 shows less significant changes in morphology thanks to the improved energy absorption characteristics compared to the other two foams (see Table 4).

The effect of the impact energy on the foam microstructure was quantified by calculating the microscopic parameters (defined in Section 4.1) for each testing condition. Furthermore, untested specimens ($J_i = 0$ J) were also analysed for reference. All parameters show similar probability distributions (see Fig. A.2) across all testing conditions: the sphericity measurements follow normal distributions (coefficient of determination, $R^2 \approx 0.95$) with comparable standard deviations, and coefficients of variations (the ratio between standard deviation and mean) lower than 0.22; therefore, the mean value was taken as indicative of each condition. The radius distribution follows an exponential law ($R^2 \approx 0.83$) and is thus described by its mean value. On the other hand, the rib tortuosity data do not follow a specific distribution function, but for consistency, the mean values were taken as representative. The effect of J_i on porosity, pore radius, pore sphericity, and ribs tortuosity is shown in Fig. 9.(b–e).

The values of porosity (ϕ) for the untested samples ($J_i = 0$ J) for RF1 and RF3 are quite similar (90.9% and 90.6%, respectively) and significantly higher than that of RF2 (83.1%). These results agree with the apparent density measurements reported in Table 1 and previous results for the same foams [21]. As expected, ϕ shows a clear, decreasing trend with increasing impact energy for all specimens: this results from the densification process, where the cell ribs are pushed closer during crushing.

For $J_i = 0$ J, the mean radius of RF1 and RF3 is almost double that of RF2, supporting the differences in mechanical response reported in Section 3. On the other hand, RF2 presents a higher sphericity than the other materials. RF1 and RF3 show a monotonic decreasing pore radius trend and a monotonic increasing pore sphericity trend. In contrast, the pore radius and sphericity trends for RF2 appear bi-modal, possibly indicating the incomplete destruction of the lower-sphericity voids at $J_i = 5$ J, which become even less spherical as they are crushed. This results in an increase in mean radius and a decrease in mean sphericity for lower impact energies.

Upon compression, the pores become less elongated and approach a more spherical and isotropic shape, as already observed [44]. This phenomenon could be preferential to the least spherical (or more elongated) voids, especially those perpendicular to the impact direction. Nonetheless, the crushing and increased sphericity of the pores results in the quasi-isotropic macroscopic material response observed at high strain levels, where negligible differences are observed in material properties between the two directions (see Fig. 6).

Finally, the rib tortuosity is close to unity for the untested samples, indicating nearly straight ribs in the foams. As the compression level increases, more ribs become curved; therefore, the mean value of τ increases accordingly. Similar results were reported by [50] during the auxetic conversion process of open-cell PU foams, where volumetric compression and heat were applied to induce a negative Poisson's ratio effect in the foams [50]. Furthermore, the trend for RF2 shows a less steep tortuosity trend than RF1 and RF3: this is most likely a result of the lower porosity degree and the thicker ribs of RF2, which are stiffer and deform less during compression.

Overall, the dependence of the microscopic parameters on the imposed impact energy highlights the hierarchical nature of RPUFs and the possibility of tuning the mechanical response by means of composition (and, therefore, microstructure) control.

5. Constitutive model

5.1. Model description

When modelling the impact response of foams, previous studies often adopted the Nagy [51] or Sherwood-Frost [52] models to account for the effects of strain rate, density and temperature. On the other hand, no significant difference in mechanical behaviour was observed in the strain rate range studied in this work, and the temperature effect was not investigated. From the results reported in Section 3, the main effect of increasing the impact energy was an increase in energy absorption and peak stress and strain. For these reasons, the constitutive model employed in this study mainly focuses on a semi-empirical approach in describing the loading–unloading response of the investigated materials.

The hyperfoam (or Ogden foam) model was adopted to describe and predict the macroscopic stress–strain response of the three RPUFs. The model was initially introduced by Ogden and Hill [53] to describe the hyperelastic behaviour of elastomers, and has been employed to reproduce the characteristic response of cellular materials [54–56]. In

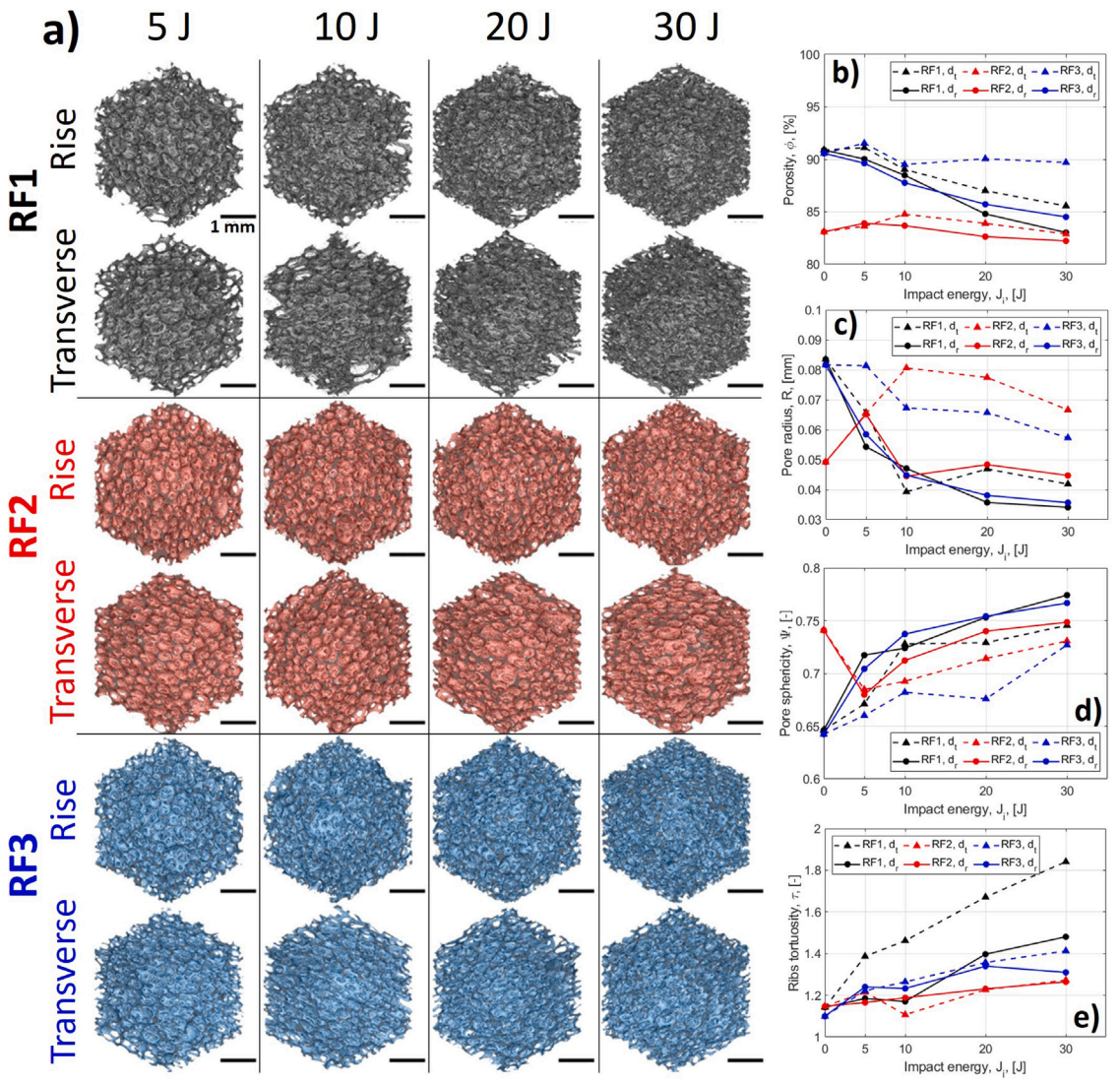

Fig. 9. (a) Micro-computed tomography (μCT) sub-volumes of the three foams (RF1, RF2, and RF3), in the rise (d_r) and transverse (d_t) directions, subjected to impact energies (J_i) of 5, 10, 20, *and*30 J. Only the rib networks are shown for clarity (scale common to all figures). Dependence of significant microstructural parameters (mean values) on the impact energy: (b) porosity (ϕ); (c) pore radius (R); (d) pore sphericity (Ψ); and (e) ribs tortuosity (τ).

the model, the strain energy function (W) is provided in terms of the three principal stretches λ_k ($\lambda_k = \varepsilon_k + 1$, with $k = 1, 2, 3$), following Eq. (9):

$$W\left(\lambda_1, \lambda_2, \lambda_3\right) = \sum_{i=1}^{N} \frac{2\mu_i}{\alpha_i^2}\left(\lambda_1^{\alpha_i} + \lambda_2^{\alpha_i} + \lambda_3^{\alpha_i} - 3 + \frac{1}{\beta_i}\left(J^{-\alpha_i\beta_i} - 1\right)\right), \tag{9}$$

where μ_i, α_i, and β_i are material coefficients, N is the number of terms in the series, and J is the volume ratio. In particular, the terms β_i determine the compressibility degree and are related to the Poisson's ratio (ν_i) as $\beta_i = \nu_i / \left(1 - 2\nu_i\right)$. In this study, all compressibility terms are considered identical ($\beta_i = \beta$) and a function of the generalised Poisson's ratio ν_0 (see Eq. (1)).

In the case of uniaxial loading, as in the drop impact tests, it is possible to show that $\lambda_1 = \lambda$ and $\lambda_2 = \lambda_3 = \lambda^{-\nu_0}$ [57,58], assuming the loading direction corresponds to the first principal direction. It follows that $J = \lambda_1\lambda_2\lambda_3 = \lambda^{1-2\nu_0}$ for the uniaxial case. The nominal stress is therefore determined from Eq. (10):

$$\sigma = \frac{\partial W(\lambda)}{\partial \lambda} = \frac{2}{\lambda}\sum_{i=1}^{N}\frac{\mu_i}{\alpha_i}\left(\lambda^{\alpha_i} - \lambda^{-\alpha_i\nu_0}\right). \tag{10}$$

Note that the model parameters are related to the initial shear modulus (G) and initial volumetric modulus (K) through Eq. (11):

$$G = \sum_{i=1}^{N}\mu_i, \qquad K = 2\sum_{i=1}^{N}\mu_i\left(\frac{1}{3} + \beta_i\right). \tag{11}$$

The hyperfoam model is suitable for predicting the loading curve of foams. On the other hand, unloading is not predicted as no damage is assumed throughout the deformation process. Ogden and Roxburgh proposed a phenomenological model to account for stress softening and hysteresis during the cyclic loading of filled elastomers [59]. A damage variable η is introduced, which affects the strain function as reported in Eq. (12):

$$\bar{W}(\lambda, \eta) = \eta W(\lambda) + \Phi(\eta), \tag{12}$$

where $\Phi(\eta)$ is a continuous damage function. The damage parameter proposed takes the form reported in Eq. (13):

$$\eta = 1 - \frac{1}{r}erf\left(\frac{W_{max} - W}{m}\right), \tag{13}$$

where r, m are fitting parameters, W_{max} is the maximum value of W along the loading path, and $erf()$ is the error function. In this case, the fitting parameters do not have a physical significance. Notice that W

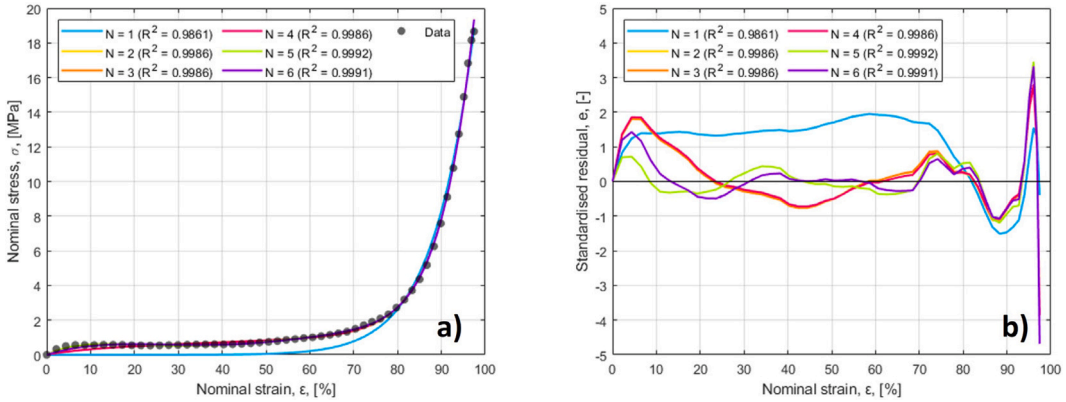

Fig. 10. Hyperfoam model calibration based on data for RF1, in the rise direction d_r, subjected to an impact energy (J_i) of 30 J. (a) Comparison of experimental data and predicted response for different model orders (N) with indication of the coefficient of determination (R^2). (b) Standardised residuals (e) plots for different model orders.

Table 6
Summary of the constitutive model ($N = 5$) parameters (μ_i, α_i, r and m) and the measured generalised Poisson's ratio (ν_0) for the three foams (RF1, RF2, RF3) in the rise (d_r) and transverse (d_t) direction (d). Values of μ_i and m are in [MPa]; ν_0, α_i, and r are dimensionless.

Foam	d	ν_0	μ_1	α_1	μ_2	α_2	μ_3	α_3	μ_4	α_4	μ_5	α_5	r	m
RF1	d_r	0.31	−3.749	6.328	7.609	−12.29	1.757	11.06	0.251	15.52	−0.81	14.14	1.031	0.063
	d_t	0.14	−1.045	11.29	2.87	8.909	6.084	−6.421	−4.479	3.785	0.021	16.83	1.057	0.075
RF2	d_r	0.28	8.972	−9.244	−5.928	−2.131	10.91	−9.199	2.105	7.456	−4.283	5.969	1.013	0.018
	d_t	0.18	27.31	−5.623	27.61	−5.604	−18.91	−3.373	0.129	10.26	−22.34	−3.331	1.036	0.029
RF3	d_r	0.43	10.56	−13.44	2.774	9.73	−1.687	12.27	0.478	13.75	−6.68	5.734	1.03	0.032
	d_t	0.17	1.158	6.272	−0.471	8.772	−0.01	11.5	0.046	8.185	0.002	18.65	1.061	0.042

corresponds to the EA defined previously in Eq. (2). During loading, $W = W_{max}$ at every increment, so that $\eta = 1$ and $\Phi(\eta = 1) = 0$. The predicted nominal stress ($\bar{\sigma}$) is obtained by derivation of Eq. (12), similarly to Eq. (10).

5.2. Parameters calibration

The constitutive model presented in Section 5.1 was calibrated by fitting the experimental nominal stress–strain curves through the function `lsqcurvefit` in MATLAB, employing a nonlinear least-squares fitting method based on the Marquardt–Levenberg algorithm [60]. The fitting accuracy of the model was quantified by calculating the coefficient of determination, R^2, and the standardised residuals, e (i.e., the difference between experimental data and model prediction, normalised by its standard deviation). The generalised Poisson's ratio (ν_0) was identified following the procedure reported in Section 2.4, and the obtained values are reported in Table 6. Only the average values of ν_0 were used for the parameters fitting.

The hyperfoam constants in Eq. (10) were determined from the loading curve of specimens subjected to $J_i = 30$ J; different hyperfoam orders were compared, ranging from $N = 1$ to $N = 6$. In contrast, previous studies [54–56] adopted a hyperfoam model with $N = 3$, which limited the analysis to the linear elastic and plateau regions of the foams' behaviour. For $N \leq 4$, the model fails to capture the complete stress–strain curves, underestimating the stress in the linear elastic region as shown in Fig. 10 for RF1 in d_r. It can also be noticed that for $N = 5$, the model presents the best R^2 and lowest residuals. The same considerations are also valid for RF2 and RF3.

For these reasons, the model order $N = 5$ was chosen as the most appropriate for the materials investigated. Finally, the Ogden–Roxburgh fitting parameters in Eq. (13) were determined from the unloading region of the curves corresponding to specimens subjected to $J_i = 30$ J. The comparison between experimental data and model prediction is reported in Fig. 11, and the model parameters are reported in Table 6.

The model approximates the calibration curves well, with limited residuals and very high R^2 (ranging from 0.9986 to 0.9994). It can be observed that the model consistently overestimates the peak stress. The hyperfoam constants were only determined from the loading curve. Therefore, some divergence might be experienced at the endpoint used for fitting (i.e., the peak stress). Furthermore, the Ogden–Roxburgh damage parameter η correctly describes the calibration curves' unloading region and residual deformation.

Table 7
Coefficient of determination (R^2) for the model prediction of the three foams (RF1, RF2, RF3) in the rise (d_r) and transverse (d_t) direction (d), subjected to different impact energies (J_i). The values refer to the curves reported in Fig. 12.

Foam	d	J_i, [J]			
		5	10	20	30
RF1	d_r	0.8273	0.7954	0.9317	0.9825
	d_t	0.8649	0.8609	0.8954	0.9824
RF2	d_r	0.9794	0.9790	0.9900	0.9876
	d_t	0.9750	0.9809	0.9567	0.9867
RF3	d_r	0.7627	0.7491	0.9765	0.9847
	d_t	0.8682	0.8738	0.9766	0.9890

5.3. Model validation

The model was validated by predicting the materials' response at lower impact energies ($J_i = 5$, 10, and 20 J) using the material constants reported in Table 6, and the results are shown in Fig. 12. Notice that the curves corresponding to $J_i = 30$ J in Fig. 12 are different from those used for the model calibration (see Fig. 11).

From Fig. 12.(b–e), it can be observed that the model predicts the response of RF2 with high accuracy in both material directions, as indicated by the $R^2 \geq 0.96$ for all conditions (see Table 7). On the other hand, the model fails to capture the difference between the curves of RF1 at $J_i = 20$ J and 30 J because the samples reach a similar deformation level but show different peak stresses. The stress for the loading curves of RF3 is predicted with reasonable accuracy. However, the peak stress is overestimated for the highest impact energy in the transverse direction (see Fig. 12.(f)), as already highlighted in Section 5.2. Overall,

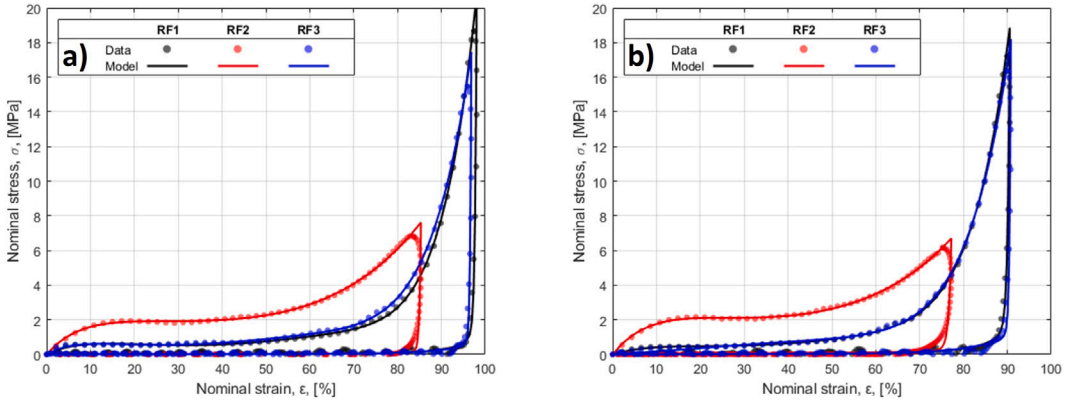

Fig. 11. Comparison between experimental data and model prediction ($N = 5$) for the three foams (RF1, RF2, RF3) subjected to an impact energy (J_i) of 30 J in the two material directions: (a) rise (d_r), (b) transverse (d_t).

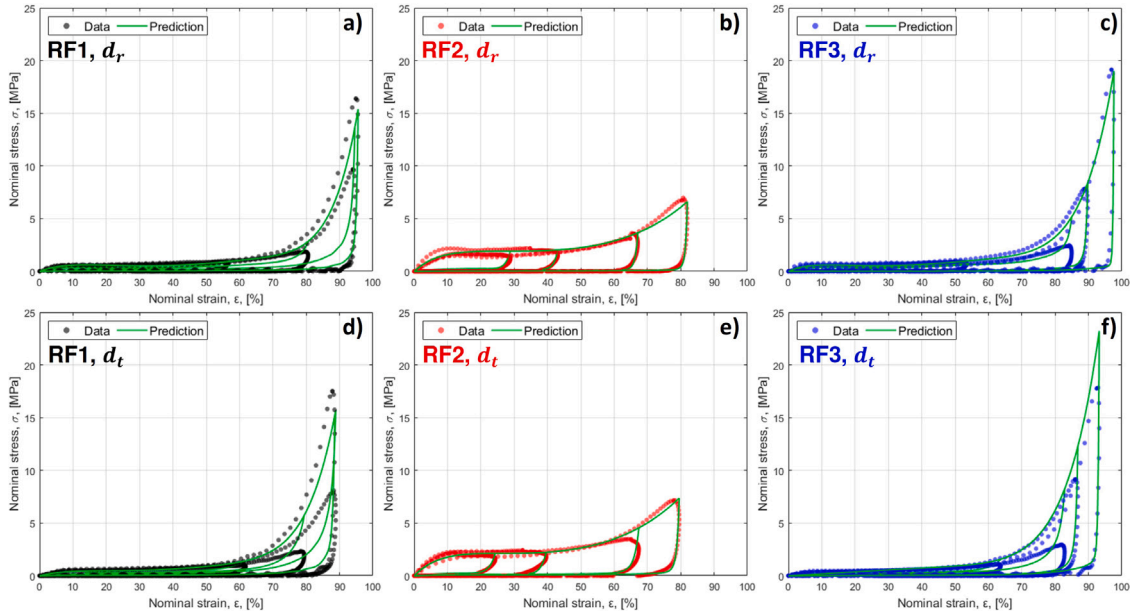

Fig. 12. Comparison between experimental data and model prediction ($N = 5$) for the three foams (RF1, RF2, RF3) in the rise (d_r) and transverse (d_t) directions subjected to different impact energies ($J_i = 5$, 10, 20, 30 J): (a) RF1, d_r; (b) RF2, d_r; (c) RF3, d_r; (d) RF1, d_t; (e) RF2, d_t; (f) RF3, d_t.

the model describes the loading curves of the three foams at different impact energies. The accuracy could be improved even further by considering the dependence of the Poisson's ratio on the strain level (as discussed in Section 2.4) instead of a constant, generalised valued ν_0. On the other hand, determining the value of ν over the deformation range experienced by the foams would be a complex experimental task, as the optical strain measurement employed in this work is unreliable for $\epsilon > 50\%$. On the other hand, the need for ten fitting constants per material direction is quite limiting for large numerical simulations, as it comes with a high computational cost. Simpler constitutive models should be considered in future work. For example, Lu et al. proposed a constitutive model based on five constants (two of which correspond to the modulus and yield stress of the material, respectively), which showed comparable accuracy to the hyperfoam model [61]. Nonetheless, both models are phenomenological and cannot be derived from micro-mechanics but only from fitting the material response.

The prediction accuracy of the unloading region and, especially, of the residual deformation is less accurate for RF1 and RF3, especially for $J_i = 5$ J and 10 J, resulting in lower coefficients of determination (see Table 7, the correlation is still acceptable as $R^2 \geq 0.75$ in all conditions). In contrast, the unloading response of RF2 is predicted with high accuracy, most likely because the calibration curve was limited to lower strains compared to RF1 and RF3. Therefore, the damage fitting parameters (r, m) can capture the unloading path also for lower impact energies. The prediction of the residual deformation is a well-known limitation of the Ogden–Roxburgh damage model [62]. The model does not explicitly define a residual strain but is limited to describing the stress-softening behaviour experienced by elastomers during cyclic loading (i.e., the Mullins effect). The values of r and m for the curves reported in Fig. 12 were determined and are reported in Tables B.2 and B.3 in Appendix B. It is evident that neither parameter follows a clear trend with increasing impact energy. Therefore, determining a function that accounts for the constants variation with J_i is quite challenging. On the other hand, Dorfmann and Ogden proposed an additional non-dimensional residual strain variable (related to the energy level and material shear modulus), which could improve the model accuracy but would require the determination of two additional fitting parameters [63].

6. Conclusions

In this work, the low-velocity impact response of three rigid polyurethane foams (RPUFs) obtained from commercially available castor oil-based resins has been characterised. In particular, the effect

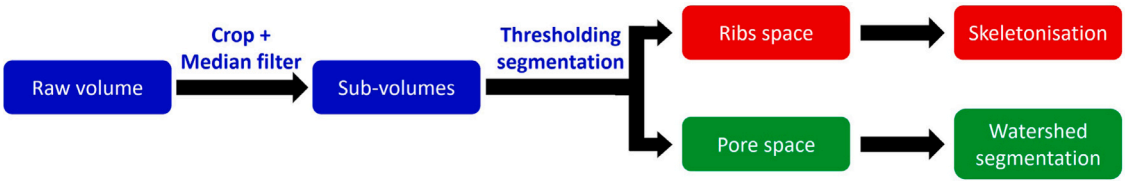

Fig. A.1. Micro-computed tomography (μCT) scans processing flowchart.

of different impact energies was investigated. The main findings are summarised as follows.

- The macroscopic impact response and energy absorption characteristics were characterised via drop weight impact tests. The results highlight favourable stiffness (compressive modulus ranging from 6 MPa for RF3, d_t to 26 MPa RF2, d_r) and energy absorption efficiency (ranging from 40% for RF2 to 45% for RF1 and RF3), making the materials suitable candidates for replacing petroleum-based foams, as already suggested in Refs. [20,21].
- The microscopic evolution of the foam morphology was investigated through an extensive μCT campaign. The findings highlight how the macro and micro scales are interconnected and influence each other: porosity and pore radius decrease with increasing impact energy. In contrast, pore sphericity and rib tortuosity show an increasing trend.
- The macroscopic mechanical response and the effect of impact energy were described and predicted through a constitutive relationship based on the hyperfoam and Ogden–Roxburgh models. The model shows a good correlation with experimental data, making it suitable for describing the material behaviour at different impact energies. However, its accuracy could be further improved by introducing additional parameters describing the effect of the impact energy on the residual deformation.

The results reported in this work help fill the gap in the available literature on the low-velocity impact response of bio-based RPUFs. Furthermore, they highlight the possibility of tuning the foam properties via composition design and control. By acting on the ratios of chemical reactants used in the foam preparation, it is possible to control its microstructure and impact response. Characterising and predicting the response of bio-based materials in different loading conditions is a necessary step in proving the feasibility of these novel foams in replacing standard materials derived from petroleum sources.

CRediT authorship contribution statement

Jacopo Lavazza: Writing – original draft, Visualization, Software, Methodology, Investigation, Funding acquisition, Formal analysis, Data curation, Conceptualization. **Qicheng Zhang:** Supervision, Software, Conceptualization. **Charles de Kergariou:** Writing – review & editing, Visualization, Supervision, Methodology. **Gianni Comandini:** Writing – review & editing, Visualization, Supervision. **Fernando Alvarez-Borges:** Writing – review & editing, Resources, Investigation, Funding acquisition. **Orestis L. Katsamenis:** Writing – review & editing, Resources, Investigation. **Wuge H. Briscoe:** Writing – review & editing, Visualization, Supervision, Conceptualization. **Jemma L. Rowlandson:** Writing – review & editing, Visualization, Supervision. **Tulio Hallak Panzera:** Supervision, Resources, Project administration, Funding acquisition, Conceptualization. **Fabrizio Scarpa:** Writing – review & editing, Visualization, Supervision, Resources, Project administration, Funding acquisition, Conceptualization.

Declaration of competing interest

The authors declare that they have no known competing financial interests or personal relationships that could have appeared to influence the work reported in this paper.

Acknowledgements

This work was supported and funded by the EPSRC Centre, UK for Doctoral Training in Composites Science, Engineering, and Manufacturing (CDT CoSEM) [EP/S021728/1] at the University of Bristol. μCT imaging was supported and funded by the EPSRC National Research Facility, UK for Lab X-ray CT (NXCT) at the μ-VIS X-ray Imaging Centre, University of Southampton [EP/T02593X/1]. CdK would like to thank the EPSRC Doctoral Prize Fellowship, UK [EP/W524414/1] for its support. FS and THP also acknowledge the support of the NEUROMETA project, UK [ERC-2020-AdG 101020715].

Appendix A. Micro-computed tomography processing and sub-volumes comparison

Fig. A.1 reports the general procedure for the analysis of the μCT volumes, as described in Section 4.1. A median filter was applied to the original volumes, then cropped into sub-volumes. Binary segmentation was performed by thresholding to selected levels and obtaining the polymeric ribs and pore space. Watershed segmentation was employed to identify and separate the individual pores. The rib space was skeletonised and converted into a sparse graph, identifying the nodes and connections of the rib network. Relevant parameters were determined according to the details in Section 4.1.

Of particular interest are the sub-volumes (500 × 500 × 500 voxels in size), which were employed to reduce the computational time of the analysis. To verify the accuracy and significance of the measurements performed on the sub-volumes, eight distinct sub-volumes (labelled S1 to S8) were obtained from the scanned volume of a sample of RF1 in the rise direction (d_r) subjected to $J_i = 5$ J. The sub-volumes were then characterised by calculating the parameters reported in Section 4.1: the distributions of ribs tortuosity (τ), pore radius (R), and pore sphericity (Ψ) are reported in Fig. A.2, alongside the sub-volumes. Furthermore, each sub-volumes' porosity (ϕ) is reported in Table A.1, with the mean and global (obtained from the raw volume) values.

Appendix B. Effect of impact energy on the damage parameter

The stress–strain curves obtained at different impact energies (J_i) reported in Fig. 12 were fitted through the model reported in Section 5.1. The hyperfoam constants were fixed to the values reported in Table 6, while the damage parameter constants (r and m, defined in Eq. (13)) were determined for each curve, improving the fitting accuracy. The values of r and m at varying J_i are reported in Tables B.2 and B.3, respectively.

Data availability

All underlying data to support the conclusions are provided within this paper.

Table A.1
Porosity (ϕ) of the sub-volumes (S1 to S8) and raw volume (global), obtained from a sample of RF1 in the rise direction (d_r) subjected to an impact energy (J_i) of 5 J.

	S1	S2	S3	S4	S5	S6	S7	S8	Mean	Global
ϕ, [%]	90	89.9	90.1	90	89.5	89.7	89.9	89.7	89.8 + 0.2	89.9

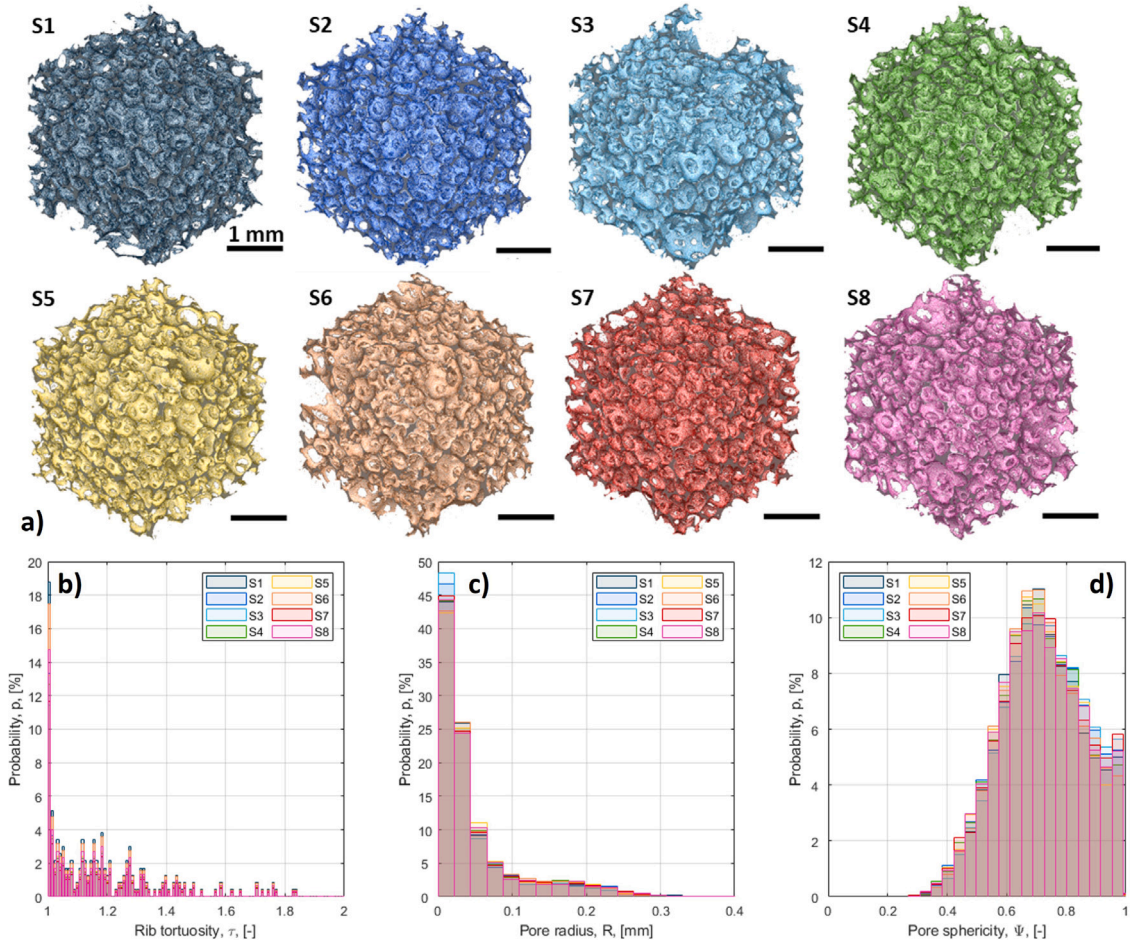

Fig. A.2. Micro-computed tomography (μCT) sub-volume analysis for a sample of RF1, in the rise direction (d_r), subjected to an impact energy (J_i) of 5 J: (a) sub-volumes (S1 to S8), only the rib networks are shown for clarity (scale common to all figures). Probability (p) distributions of: (b) ribs tortuosity (τ); (c) pore radius (R); (d) pore sphericity (Ψ).

Table B.2
Damage parameter (η, defined in Eq. (13)) fitting constant r for the three foams (RF1, RF2, and RF3) in the rise (d_r) and transverse (d_t) direction (d), subjected to different impact energies (J_i). The values refer to the curves reported in Fig. 12.

Foam	d	J_i, [J]			
		5	10	20	30
RF1	d_r	0.958	1.086	1.077	0.991
	d_t	1.080	0.968	1.095	1.006
RF2	d_r	1.082	0.919	0.993	1.005
	d_t	0.962	0.872	1.045	1.021
RF3	d_r	1.024	1.062	1.030	0.995
	d_t	1.145	1.085	1.107	1.060

Table B.3
Damage parameter (η, defined in Eq. (13)) fitting constant m for the three foams (RF1, RF2, and RF3) in the rise (d_r) and transverse (d_t) direction (d), subjected to different impact energies (J_i). The values refer to the curves reported in Fig. 12.

Foam	d	J_i, [J]			
		5	10	20	30
RF1	d_r	0.0143	0.0037	0.0095	0.0652
	d_t	0.0137	0.0004	0.0010	0.0750
RF2	d_r	0.0085	0.0228	0.0231	0.0272
	d_t	0.0284	0.0529	0.0133	0.0390
RF3	d_r	0.0062	0.0003	0.0263	0.0664
	d_t	0.0051	0.0002	0.0122	0.0375

References

[1] Koohbor B, Kidane A, Lu W-Y. Effect of specimen size, compressibility and inertia on the response of rigid polymer foams subjected to high velocity direct impact loading. Int J Impact Eng 2016;98:62–74. http://dx.doi.org/10.1016/j.ijimpeng.2016.08.006.

[2] Li P, Guo YB, Zhou MW, Shim VPW. Response of anisotropic polyurethane foam to compression at different loading angles and strain rates. Int J Impact Eng 2019;127:154–68. http://dx.doi.org/10.1016/j.ijimpeng.2018.12.009.

[3] Avalle M, Belingardi G, Montanini R. Characterization of polymeric structural foams under compressive impact loading by means of energy-absorption diagram. Int J Impact Eng 2001;25(5):455–72. http://dx.doi.org/10.1016/S0734-743X(00)00060-9.

[4] Shim V, Tu Z, Lim C. Two-dimensional response of crushable polyurethane foam to low velocity impact. Int J Impact Eng 2000;24(6–7):703–31. http://dx.doi.org/10.1016/S0734-743X(99)00149-9.

[5] Chen W, Lu F, Winfree N. High-strain-rate compressive behavior of a rigid polyurethane foam with various densities. Exp Mech 2002;42(1):65–73. http://dx.doi.org/10.1007/BF02411053.

[6] Zhang G, Wang B, Ma L, Wu L, Pan S, Yang J. Energy absorption and low velocity impact response of polyurethane foam filled pyramidal lattice core sandwich panels. Compos Struct 2014;108:304–10. http://dx.doi.org/10.1016/j.compstruct.2013.09.040.

[7] Pellegrino A, Tagarielli VL, Gerlach R, Petrinic N. The mechanical response of a syntactic polyurethane foam at low and high rates of strain. Int J Impact Eng 2015;75:214–21. http://dx.doi.org/10.1016/j.ijimpeng.2014.08.005.

[8] Mane JV, Chandra S, Sharma S, Ali H, Chavan VM, Manjunath BS, Patel RJ. Mechanical property evaluation of polyurethane foam under quasi-static and dynamic strain rates- An experimental study. Procedia Eng 2017;173:726–31. http://dx.doi.org/10.1016/j.proeng.2016.12.160.

[9] Hwang B-K, Kim S-K, Kim J-H, Kim J-D, Lee J-M. Dynamic compressive behavior of rigid polyurethane foam with various densities under different temperatures. Int J Mech Sci 2020;180:105657. http://dx.doi.org/10.1016/j.ijmecsci.2020.105657.

[10] Zhang Z, Zhong W, Chen J, Luo J. Compressive properties and energy absorption of rigid polyurethane foam. J Phys: Conf Ser 2022;2368(1):012013. http://dx.doi.org/10.1088/1742-6596/2368/1/012013.

[11] Helling RK, Russell DA. Use of life cycle assessment to characterize the environmental impacts of polyol production options. Green Chem 2009;11(3):380–9. http://dx.doi.org/10.1039/B815833A.

[12] Recupido F, Lama GC, Ammendola M, Bossa FDL, Minigher A, Campaner P, Morena AG, Tzanov T, Ornelas M, Barros A, Gomes F, Bouça V, Malgueiro R, Sanchez M, Martinez E, Sorrentino L, Boggioni L, Perucca M, Anegalla S, Marzella R, Moimare P, Verdolotti L. Rigid composite bio-based polyurethane foams: From synthesis to LCA analysis. Polymer 2023;267:125674. http://dx.doi.org/10.1016/j.polymer.2023.125674.

[13] Lee JH, Kim SH, Oh KW. Bio-based polyurethane foams with castor oil based multifunctional polyols for improved compressive properties. Polym (Basel) 2021;13(4):576. http://dx.doi.org/10.3390/polym13040576.

[14] Fridrihsone A, Romagnoli F, Kirsanovs V, Cabulis U. Life cycle assessment of vegetable oil based polyols for polyurethane production. J Clean Prod 2020;266:121403. http://dx.doi.org/10.1016/j.jclepro.2020.121403.

[15] Mubofu EB. Castor oil as a potential renewable resource for the production of functional materials. Sustain Chem Process 2016;4(1):11. http://dx.doi.org/10.1186/s40508-016-0055-8.

[16] Cabulis U, Ivdre A. Recent developments in the sustainability of the production of polyurethane foams from polyols based on the first- to the fourth-generation of biomass feedstock. Curr Opin Green Sustain Chem 2023;44:100866. http://dx.doi.org/10.1016/j.cogsc.2023.100866.

[17] Jeyanthi S, Nivedhitha DM, Jeyamani E, Lazar PJL, Krishnaswamy P. Experimental and numerical study of rigid polyurethane foams for mechanical characteristics using finite element analysis. J Phys: Conf Ser 2023;2601(1):012028. http://dx.doi.org/10.1088/1742-6596/2601/1/012028.

[18] Singh S, Sharma S, Sarma SJ, Brar SK. A comprehensive review of castor oil-derived renewable and sustainable industrial products. Environ Progress Sustain Energy 2023;42(2):e14008. http://dx.doi.org/10.1002/ep.14008.

[19] Srinivasan V, Vasam S, Govindarajan S. Improved thermal and mechanical properties of water-blown rigid polyurethane foams synthesized with renewable castor oil and toluene diisocyanate-based trifunctional polyols. Cell Polym 2023;42(5–6):226–37. http://dx.doi.org/10.1177/02624893231204620.

[20] Soares LF, dos Santos JC, de Freitas VAA, Pereira RBD, Panzera TH, Scarpa F. Castor-oil biobased foam: The effect of the composition on the physical and mechanical properties via a statistical mixture design. RSC Sustain 2024;2(4):975–87. http://dx.doi.org/10.1039/D3SU00374D.

[21] Lavazza J, Zhang Q, De Kergariou C, Comandini G, Briscoe WH, Rowlandson JL, Panzera TH, Scarpa F. Rigid polyurethane foams from commercial castor oil resins. Polym Test 2024;135:108457. http://dx.doi.org/10.1016/j.polymertesting.2024.108457.

[22] Mourão RP, Neto MM. The use of castor oil polyurethane foam in impact limiters for radioactive materials packages. Int J Radioact Mater Transp 2003;14(1):49–62. http://dx.doi.org/10.1179/rmt.2003.14.1.49.

[23] Martin U, Mosler U, Lehmhus D, Müller A, Heinzel G. Hierarchical structure of aluminium foams and relation to compression behaviour. High Temp Mater Process 2007;26(4):291–6. http://dx.doi.org/10.1515/HTMP.2007.26.4.291.

[24] Rahimidehgolan F, Altenhof W. Compressive behavior and deformation mechanisms of rigid polymeric foams: A review. Composites B 2023;253:110513. http://dx.doi.org/10.1016/j.compositesb.2023.110513.

[25] Elliott JA, Windle AH, Hobdell JR, Eeckhaut G, Oldman RJ, Ludwig W, Boller E, Cloetens P, Baruchel J. In-situ deformation of an open-cell flexible polyurethane foam characterised by 3D computed microtomography. J Mater Sci 2002;37(8):1547–55. http://dx.doi.org/10.1023/A:1014920902712.

[26] Kartal ME, Dugdale LH, Harrigan JJ, Siddiq MA, Pokrajac D, Mulvihill DM. Three-dimensional in situ observations of compressive damage mechanisms in syntactic foam using X-ray microcomputed tomography. J Mater Sci 2017;52(17):10186–97. http://dx.doi.org/10.1007/s10853-017-1177-4.

[27] Patterson BM, Henderson K, Gilbertson RD, Tornga S, Cordes NL, Chavez ME, Smith Z. Morphological and performance measures of polyurethane foams using X-Ray CT and mechanical testing. Microsc Microanal 2014;20(4):1284–93. http://dx.doi.org/10.1017/S1431927614000993.

[28] De Schryver T, Dierick M, Heyndrickx M, Van Stappen J, Boone MA, Van Hoorebeke L, Boone MN. Motion compensated micro-CT reconstruction for in-situ analysis of dynamic processes. Sci Rep 2018;8(1):7655. http://dx.doi.org/10.1038/s41598-018-25916-5.

[29] Zhang Q, Scarpa F, Barton D, Zhu Y, Lang Z-Q, Zhang D, Peng H-X. Impact properties of uniaxially thermoformed auxetic foams. Int J Impact Eng 2022;163:104176. http://dx.doi.org/10.1016/j.ijimpeng.2022.104176.

[30] Katsamenis OL, Basford PJ, Robinson SK, Boardman RP, Konstantinopoulou E, Lackie PM, Page A, Ratnayaka JA, Goggin PM, Thomas GJ, Cox SJ, Sinclair I, Schneider P. A high-throughput 3D X-ray histology facility for biomedical research and preclinical applications [version 2; peer review: 3 approved, 1 approved with reservations]. Wellcome Open Res 2023;8(366). http://dx.doi.org/10.12688/wellcomeopenres.19666.2.

[31] Roh JH, Giller CB, Mott PH, Roland CM. Failure of classical elasticity in auxetic foams. AIP Adv 2013;3(4):042126. http://dx.doi.org/10.1063/1.4802925.

[32] Rinde JA. Poisson's ratio for rigid plastic foams. J Appl Polym Sci 1970;14(8):1913–26. http://dx.doi.org/10.1002/app.1970.070140801.

[33] Schindelin J, Arganda-Carreras I, Frise E, Kaynig V, Longair M, Pietzsch T, Preibisch S, Rueden C, Saalfeld S, Schmid B, Tinevez J-Y, White DJ, Hartenstein V, Eliceiri K, Tomancak P, Cardona A. Fiji: An open-source platform for biological-image analysis. Nat Methods 2012;9(7):676–82. http://dx.doi.org/10.1038/nmeth.2019.

[34] de Kergariou C, Saidani-Scott H, Perriman A, Scarpa F, Le Duigou A. The influence of the humidity on the mechanical properties of 3D printed continuous flax fibre reinforced poly(lactic acid) composites. Composites A 2022;155:106805. http://dx.doi.org/10.1016/j.compositesa.2022.106805.

[35] Xing Y, Sun D, Zhang M, Shu G. Crushing responses of expanded polypropylene foam. Polym (Basel) 2023;15(9):2059. http://dx.doi.org/10.3390/polym15092059.

[36] Miltz J, Gruenbaum G. Evaluation of cushioning properties of plastic foams from compressive measurements. Polym Eng Sci 1981;21(15):1010–4. http://dx.doi.org/10.1002/pen.760211505.

[37] Li QM, Magkiriadis I, Harrigan JJ. Compressive strain at the onset of densification of cellular solids. J Cell Plast 2006;42(5):371–92. http://dx.doi.org/10.1177/0021955X06063519.

[38] Kim T-R, Shin JK, Goh TS, Kim H-S, Lee JS, Lee C-S. Modeling of elasto-viscoplastic behavior for polyurethane foam under various strain rates and temperatures. Compos Struct 2017;180:686–95. http://dx.doi.org/10.1016/j.compstruct.2017.08.032.

[39] Viot P. Hydrostatic compression on polypropylene foam. Int J Impact Eng 2009;36(7):975–89. http://dx.doi.org/10.1016/j.ijimpeng.2008.11.010.

[40] Park S-B, Lee C-S, Choi S-W, Kim J-H, Bang C-S, Lee J-M. Polymeric foams for cryogenic temperature application: Temperature range for non-recovery and brittle-fracture of microstructure. Compos Struct 2016;136:258–69. http://dx.doi.org/10.1016/j.compstruct.2015.10.002.

[41] Shim V, Yap K. Static and impact crushing of layered foam-plate systems. Int J Mech Sci 1997;39(1):69–86. http://dx.doi.org/10.1016/0020-7403(96)00010-0.

[42] Tu Z, Shim V, Lim C. Plastic deformation modes in rigid polyurethane foam under static loading. Int J Solids Struct 2001;38(50–51):9267–79. http://dx.doi.org/10.1016/S0020-7683(01)00213-X.

[43] Ferreira ES, Rezende CA. Simple preparation of cellulosic lightweight materials from eucalyptus pulp. ACS Sustain Chem Eng 2018;6(11):14365–73. http://dx.doi.org/10.1021/acssuschemeng.8b03071.

[44] Bolintineanu DS, Waymel R, Collis H, Long KN, Quintana EC, Kramer SLB. Anisotropy evolution of elastomeric foams during uniaxial compression measured via in-situ X-ray computed tomography. Mater 2021;18:101112. http://dx.doi.org/10.1016/j.mtla.2021.101112.

[45] Park K-B, Kim H-T, Her N-Y, Lee J-M. Variation of mechanical characteristics of polyurethane foam: Effect of test method. Mater (Basel) 2019;12(17):2672. http://dx.doi.org/10.3390/ma12172672.

[46] Xiao Y, Yin J, Zhang X, An X, Xiong Y, Sun Y. Mechanical performance and cushioning energy absorption characteristics of rigid polyurethane foam at low and high strain rates. Polym Test 2022;109:107531. http://dx.doi.org/10.1016/j.polymertesting.2022.107531.
[47] Otsu N. A threshold selection method from gray-level histograms. IEEE Trans Syst Man Cybern 1979;9(1):62–6. http://dx.doi.org/10.1109/TSMC.1979.4310076.
[48] Ghazi A, Berke P, Tiago C, Massart TJ. Computed tomography based modelling of the behaviour of closed cell metallic foams using a shell approximation. Mater Des 2020;194:108866. http://dx.doi.org/10.1016/j.matdes.2020.108866.
[49] Kosmela P, Suchorzewski J, Formela K, Kazimierski P, Haponiuk JT, Piszczyk Ł. Microstructure–property relationship of polyurethane foams modified with baltic sea biomass: Microcomputed tomography vs. scanning electron microscopy. Materials 2020;13(24):5734. http://dx.doi.org/10.3390/ma13245734.
[50] Zhang Q, Lu W, Scarpa F, Barton D, Rankin K, Zhu Y, Lang Z-Q, Peng H-X. Topological characteristics and mechanical properties of uniaxially thermoformed auxetic foam. Mater Des 2021;211:110139. http://dx.doi.org/10.1016/j.matdes.2021.110139.
[51] Nagy A, Ko W, Lindholm U. Mechanical behavior of foamed materials under dynamic compression. J Cell Plast 1974;10(3):127–34. http://dx.doi.org/10.1177/0021955X7401000306.
[52] Sherwood JA, Frost CC. Constitutive modeling and simulation of energy absorbing polyurethane foam under impact loading. Polym Eng Sci 1992;32(16):1138–46. http://dx.doi.org/10.1002/pen.760321611.
[53] Ogden RW, Hill R. Large deformation isotropic elasticity – on the correlation of theory and experiment for incompressible rubberlike solids. Proc R Soc A 1972;326(1567):565–84. http://dx.doi.org/10.1098/rspa.1972.0026.
[54] Islam M, Tudryn G, Bucinell R, Schadler L, Picu R. Stochastic continuum model for mycelium-based bio-foam. Mater Des 2018;160:549–56. http://dx.doi.org/10.1016/j.matdes.2018.09.046.
[55] Kim S, Shin H, Rhim S, Rhee KY. Calibration of hyperelastic and hyperfoam constitutive models for an indentation event of rigid polyurethane foam. Composites B 2019;163:297–302. http://dx.doi.org/10.1016/j.compositesb.2018.11.045.
[56] Yan S, Jia D, Yu Y, Wang L, Qiu Y, Wan Q. Novel strategies for parameter fitting procedure of the Ogden hyperfoam model under shear condition. Eur J Mech A Solids 2021;86:104154. http://dx.doi.org/10.1016/j.euromechsol.2020.104154.
[57] Blatz PJ, Ko WL. Application of finite elastic theory to the deformation of rubbery materials. Trans Soc Rheol 1962;6(1):223–52. http://dx.doi.org/10.1122/1.548937.
[58] Ciambella J, Saccomandi G. A continuum hyperelastic model for auxetic materials. Proc R Soc Lond Ser A Math Phys Eng Sci 2014;470(2163):20130691. http://dx.doi.org/10.1098/rspa.2013.0691.
[59] Ogden RW, Roxburgh DG. A pseudo–elastic model for the Mullins effect in filled rubber. Proc R Soc Lond Ser A Math Phys Eng Sci 1999;455(1988):2861–77. http://dx.doi.org/10.1098/rspa.1999.0431.
[60] Twizell EH, Ogden RW. Non-linear optimization of the material constants in Ogden's stress-deformation function for incompressinle isotropic elastic materials. ANZIAM J 1983;24(4):424–34. http://dx.doi.org/10.1017/S0334270000003787.
[61] Lu F-d, Hua G-j, Wang L-s, Jiang H-y, Gao D. A phenomenological constitutive modelling of polyethylene foam under multiple impact conditions. Packag Technol Sci 2019;32(7):367–79. http://dx.doi.org/10.1002/pts.2445.
[62] Fazekas B, Goda TJ. Constitutive modelling of rubbers: Mullins effect, residual strain, time-temperature dependence. Int J Mech Sci 2021;210:106735. http://dx.doi.org/10.1016/j.ijmecsci.2021.106735.
[63] Dorfmann A, Ogden R. A constitutive model for the Mullins effect with permanent set in particle-reinforced rubber. Int J Solids Struct 2004;41(7):1855–78. http://dx.doi.org/10.1016/j.ijsolstr.2003.11.014.